POLITECNICO DI TORINO

Master's Degree in Nanotechnologies for ICTs

Master's Degree Thesis

Development of a Novel Simultaneous Information and Power Transfer System to Inductively Address Miniaturized Neural Implants

Supervisors:

Prof. Danilo DEMARCHI

Prof. Sandro CARRARA

Prof. Diego GHEZZI

Co-Supervisors:

Prof. Matteo COCUZZA

Eng. Gian Luca BARBRUNI

Dr. Paolo MOTTO ROS

Candidate:

Barbara GENTILE

October 2021

Al nonno Sandro

Acknowledgements

A conclusione di questa tesi e di questo lungo percorso da studentessa, vorrei dedicare qualche semplice parola per ringraziare chi ha contribuito alla mia crescita personale e chi mi è stato vicino in ogni momento.
Per cominciare, ringrazio i miei relatori Danilo Demarchi, Diego Ghezzi e Sandro Carrara e i miei correlatori Matteo Cocuzza, Paolo Motto Ros e Gian Luca Barbruni per la grande opportunità che mi hanno dato. Dare il mio contributo a questo progetto è stato un enorme piacere e fonte di orgoglio. Vi ringrazio tanto per il vostro tempo e per tutti i preziosi insegnamenti e consigli, non solo didattici, che mi avete dato.
Ringrazio enormemente tutta la mia famiglia per la presenza e l'interesse e perché con il vostro supporto e il vostro incoraggiamento mi fate sentire forte e determinata. Un immenso grazie va al nonno Sandro, primo ingegnere della famiglia e grande esempio per tutti. Grazie nonno per avermi dato sempre la grinta e per aver sempre creduto nella tua "unica nipotina femmina". Sei davvero una fonte d'ispirazione.
Grazie infinito ai miei genitori, per avermi sempre accompagnata nelle mie scelte e per essermi stati vicini in ogni singolo istante della mia vita. Questo traguardo è merito di tutti i vostri insegnamenti e sacrifici e non smetterò mai di esservene grata. Grazie mamma. Grazie papà.
Un grande grazie va a mio fratello Ricky, che mi trasmette tanta sicurezza, mi aiuta ad affrontare ogni situazione con più leggerezza e mi fa sentire importante. Ti voglio bene, anche quando litighiamo.
Ringrazio i miei grandi amici, Dadda e Ste, per essere cresciuti con me e per avermi supportata costantemente. Durante questi anni ho sempre potuto contare su di voi e sono più che sicura che questo non cambierà mai.
Grazie ai miei super coinquilini Dario ed Elisabetta. Con voi ogni giorno è stato davvero speciale e non mi avete mai fatto mancare l'aria di casa. Grazie per le chiacchierate, per essere dei sinceri confidenti e per essere degli amici eccezionali.
Ringrazio tanto Marcello, per essere un solido punto di riferimento e grande fonte di stimoli per la mia persona. Grazie per avermi sempre ascoltata, sostenuta e aiutata nei momenti di difficoltà. Grazie per il bel tempo trascorso insieme, per la fiducia reciproca, per l'affetto che mi hai dimostrato ogni giorno e anche per essere un ottimo chef.

Grazie Davide, compagno di classe insostituibile e amico fenomenale. È stato bello intraprendere questo percorso di magistrale con te e ammetto che mi mancherà tantissimo essere la tua vicina di banco.
Un grande grazie a tutti gli amici incontrati durante l'università, gli amici di biotech, gli amici della triennale e della magistrale. Avete reso ogni sfida più divertente ed è stato un onore per me condividere ogni momento importante con voi.
Ringrazio infine tutti gli amici del laboratorio per aver reso il semestre di tesi così piacevole, in particolare Simone per avermi aiutata a mantenere la calma quando "non funzionava niente" e Leo per i saggi consigli.
Un sincero grazie a tutte le persone citate e a tutti coloro che mi sono stati vicini durante questo percorso, ve ne sono immensamente grata.

Abstract

Implantable medical devices have experienced a major development in the past years due to the super-miniaturization of mechanical structures and electronic circuits. Among the most innovative medical technologies, "Neural Dust" and "Body Dust" are two key concepts in the field of neural bio-implants for brain recording and spreadable bio-electronics for marker sensing respectively. Moreover, neurostimulation is a promising method to address several neurological and mental disorders. Toward this end, the project carried at Medtronic Chair in Neuroengineering (EPFL, Genève) and Integrated Circuits Laboratory (EPFL, Neuchâtel) aims to restore the sense of vision in blind patients. Brain implantation is challenging and the main target is to design a device less invasive as possible. To accomplish the minimal invasive intention, the best course of action is to send power and data from an external transmitter, avoiding the introduction of wires that easily lead to scarring and infections.

In this work, a printed circuit board has been designed, fabricated and characterized starting from the study of Barbruni *et al.* [1] and optimizing it, redesigning the schematic around the components and inserting a microcontroller to exploit its serial peripheral interface. The PCB is a radiofrequency transmitter operating at 433.92 MHz with an amplitude-shift keying modulator that modulates the amplitude accordingly to the digital data, received from image processing, to individually address the implanted CMOS µelectrodes with the correct intensity. In addition to the PCB, a study of the 3-coil inductive link has been done with electromagnetic simulations, in particular to discover the best shape for the implanted secondary coil: the resonator. The coil with the highest quality factor, i.e. capability to boost electromagnetic field, was found to be a circular coil with 9 mm of diameter and 4 mm wide, encapsulated in biocompatible polydimethylsiloxane (PDMS). The resonator was consequently fabricated in cleanroom with 200 µm of encapsulating PDMS and then tested to verify the match with simulations. Moreover, some transmitting coils were printed to further test the transmitter. The results are promising, the PCB output is the expected one with small attenuations that have been adjusted in a new PCB design. The shape of the resonator with highest quality factor was found, the feasibility of its fabrication was confirmed and the measurements have proved that the simulations are reliable.

Table of Contents

List of Tables

List of Figures

Acronyms

AMD
: Age-related Macular Degeneration

APT
: Acoustic Power Transfer

ASK
: Amplitude-Shift Keying

BMI
: Brain Machine Interface

CMOS
: Complementary Metal-Oxide Semiconductor

CPT
: Capacitive Power Transfer

CS
: Chip Select

DSO
: Digital Storage Oscilloscope

IEU
: Implantable Electronic Unit

IMD
: Implantable Medical Device

IPG
: Implantable Pulse Generator

IPT
: Inductive Power Transfer

ISM
: Industrial, Scientific and Medical

LDO
: Low-Dropout

LSB
: Least Significant Bit

MCU
: Microcontroller Unit

MEA
: Microelectrodes Array

MISO
: Master Input Slave Output

MOSI
: Master Output Slave Input

MSB
: Most Significant Bit

PA
: Power Amplifier

PCB
: Printed Circuit Board

PDL
: Power Delivered to the Load

PDMS
: Polydimethylsiloxane

PGMEA

Propylene Glycol Monomethyl Ether Acetate

PLL

Phase-Locked Loop

PSS

Polystyrene Sulfonate

PTE

Power Transfer Efficiency

RF

Radiofrequency

RFID

Radio Frequency Identification

RP

Retinis Pigmentosa

SAR

Specific Absorption Rate

SCLK

Serial Clock

SDI

Serial Data Input

SDO

Serial Data Output

SIMO

Slave Input Master Output

SMA

Subminiature version A

SOMI

Slave Output Master Input

SPI

Serial Protocol Interface

SRF

Self Resonance Frequency

SS

Slave Select

SWIPT

Simultaneous Wireless Information and Power Tranfer

TEM

Transverse Electromagnetic

USCI

Universal Serial Communication Interface

WPT

Wireless Power Transfer

Chapter 1

Introduction: The Great Progress of Implantable Medical Devices

Implantable medical devices (IMD) have experienced a major progress in the past seven decades and the development will continue due to the super-aged society. Nowadays 5% to 6% of the people living in an industrialized country have been through a surgical or medical procedure to introduce, partially or totally, an implantable device in their bodies. The IMDs range from pacemakers, defibrillators and sensors to brain, nerve and bone stimulators [2]. The significant progress of implantable devices is strictly linked to the growing knowledge of the neuro-motor system and the spread, from the 1960s, of cleanroom facilities which have allowed the super-miniaturization of mechanical structures and electronic circuits [3].

1.1 The Impact of Neural Stimulation

Implantable microsystems that stimulate the nervous system or record neural activities are defined as neural prostheses. The complex chemical and electrical mechanisms that occur across the neural network are responsible for a wide number of stimuli. Modulating the neural function, it is possible to address health conditions, such as neuromuscular and neuropsychiatric diseases or sense organ disturbs. From the 50s, it became clear that the use of microelectrodes arrays (MEA) was considerably useful to understand the complex neural networks. In 1965, J. L. Moll, a professor from Stanford California, suggested to use the innovative techniques of Bell Telephone Laboratories, such as lithography and silicon etching, to produce arrays of electrodes to record simultaneously many points of the tissues, with little damage [4]. The research for the development of implantable prosthetic devices began in those years with implantation of electrodes arrays in the auditory nerve and the cochlea, in the inferior colliculus and in the visual cortex. Early experiments were difficult, mostly because of the inferior knowledge of the hardware required for those new application. Today, neural prosthesis seem to be a real miracle for people and all the effort that has been put to build electronic and chemical interfaces with the cellular world has brought to a deep understanding of the neural system.

1.1.1 Concept and Story of Neural Dust

The concept of Smart Dust was introduced in August 1999 by Kahn, Katz and Pister at University of California, Berkeley, with the intend to explore the limits on size and power consumption in sensor nodes [5]. The idea of the researchers was to achieve impressive performances in sensing, communication, computing hardware and power supply in a few cubic millimeters volume. The research has continued until nowadays with two branches: brain monitoring and stimulation (Neural Dust) and metabolism monitoring (Body Dust). The first work proposing a new brain machine interface (BMI) with the name of "Neural Dust", was published in 2013 [6], with the goal of developing free-floating sensory nodes with lateral-size of 10 to 100 µm. The concept was validated but the device was mm-scale and implanted in the peripheral nervous system instead of the brain. Applications into the brain, and particularly into human brain, are a goal that has not been reached yet [7].

1.1.2 Visual Prostheses

Visual impairment is classified as one of the ten most frequent causes of disabilities [8]. In 2020, in occasion of "VISION 2020: The Right to Sight", a global initiative for blindness prevention between WHO and the International Agency for the Prevention of Blindness, it was estimated that 43.3 million people were blind worldwide. A meaningful percentage of these is unavoidable [9]. The most severe visual dysfunctions are due to injuries or retinal degenerative diseases such as age-related macular degeneration (AMD) and retinis pigmentosa (RP). These two diseases avoid the conversion of light into an electrical signal, which is necessary for cortical stimulation. Currently, many researchers are working to find solutions to restore the sense of vision in blind people, giving the electrical signal from the external with the aim of visual prosthesis.
The idea of artificial vision was proposed already in 1752 with Benjamin Franklin, who claimed that hearing and sight could have been restored with electricity [10]. Few years later, in 1755, the sense restoring was investigated by Charles Leroy who wrapped a conductive wire around a blind volunteer evoking visual disturbances [11]. Those first experiments were the begin of a long journey of 200 years towards

real artificial vision devices. Between the most inspired individuals we find Dobelle who spent three decades to prove that it was possible to produce phosphenes with electrical pulses in the cortex. In 1976, Dobelle published that, he and his team, succeeded in helping a blind volunteer to read braille, cortically generating phosphenes at 30 letters per minute [12].

Loss of vision can be the result of any alteration of one or more elements in the visual pathway, hence the approaches that have been exploited as visual prosthesis are classified in cortical, lateral geniculate nucleus, optic nerve or retinal prosthesis (Fig. 1.1) [13]. Retina electrical stimulation is achieved with epiretinal, subretinal, or suprachoroidal electrode arrays. This method is one of the preferred ones because it takes advantage of the natural information processing that occurs along the visual path. However, retinal prosthesis can only treat diseases affecting photoreceptors, while stimulating the cortex allows to address any alteration occurring somewhere in the visual path, before the stimulation point (e.g. glaucoma, optic atrophy, traumatic damages) [14].
Cortical prostheses have great potential: they extend to all causes of visual impairment; the large area of the cortex allows to place a large number of stimulating electrodes offering higher resolution and the implantation is a relatively straightforward procedure [13].

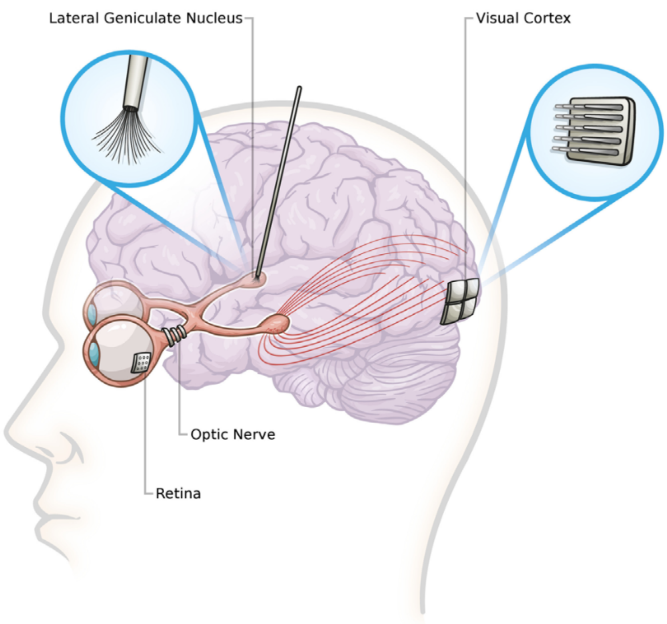

Figure 1.1: Loss of vision treated with different approaches along the visual path. Reprinted from [13].

1.2 Challenges of implants

Several requirements should be addressed when designing a medical implant: small weight and size, low power consumption, high reliability, biocompatibility and minimal toxicity, high data rate and data latency. What mostly influences the desirable characteristics of the IMDs is the comfort and safety of the patients. Small and light devices will result in a less invasive surgical implantation as well as easier healing and use. Low power consumption and dissipation are necessary for long-term performances and to avoid the damaging and overstimulation of the tissues. Between the most addressed challenges one can find the way of providing energy. The use of batteries and cables can provoke long-term scarring and complex surgical intervention, while devices powered by radiofrequency (RF) links are much comfortable but the designer must consider the specific absorption rate (SAR) of the tissues to avoid permanent damages. Device reliability is also fundamental, device maintenance is difficult and a malfunctioning device can easily lead even to the death of the patient. Reliability is improved with a solid encapsulation and packaging to protect the indwelling module from the external environment. The materials exposed to the tissues must be biocompatible, otherwise the body would react with severe infections [2].

1.3 Overview of the Project: Smart Neural Dust to Revert Blindness

The aim of the research is to develop an array of thousand of individually addressable complementary metal-oxide semiconductor µelectrodes (CMOS µelectrodes) to wirelessly stimulate the visual cortex. The whole system is made as follows:

1. **Video Camera and Image Processing**: An external camera records the images that are subsequently processed and segmented to address the correct region of the cortex with the appropriate intensity;

2. **RF SWIPT Base Station**: The "radiofrequency simultaneous wireless information and power transfer base station" consists in a printed circuit that generates, modulates and amplifies the signal that will be sent to the receivers, accordingly to the digital values received from image processing;

3. **3-Coils Inductive Link**: The wireless power transfer system is an inductive link composed by a transmitter connected to the base station, a resonator implanted in the brain and a receiving coil placed in the CMOS stimulating µelectrode;

4. **CMOS Implants**: Miniaturized CMOS µelectrodes stimulate a population of neurons inducing phosphene perception.

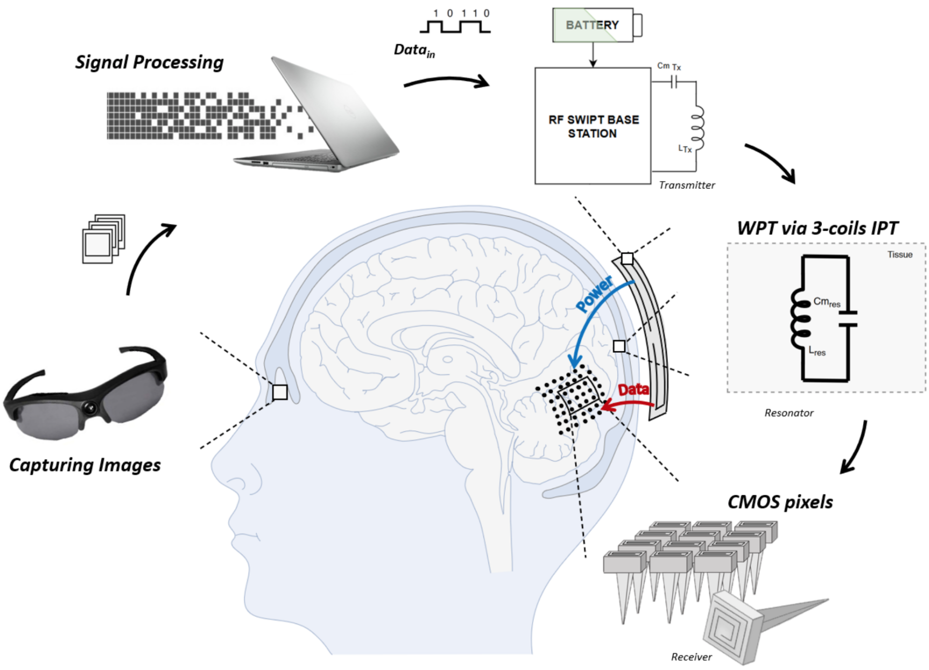

Figure 1.2: Smart Neural Dust to Revert Blindness.

1.3.1 Outline of the Master Thesis

The aim of the thesis is to design, manufacture and test a printed circuit board (PCB) for the RF SWIPT base station, starting from the work of Barbruni *et al.* [1] and to study the most efficient inductive link to achieve data and power transmission from the PCB to multiple miniaturised implanted receivers. In Chapter 2, the theory of PCB design and wireless power transfer is presented to give a detailed overview of the parameters that must be considered. In Chapter 3, all the blocks of the PCB are described together with layout strategies implemented in Altium Designer, while the results are presented in Chapter 4. In Chapter 5, the study on the inductive link is illustrated with simulations on Ansys HFSS and the fabrication of the resonator in cleanroom. The results obtained from the study of inductive link are presented in Chapter 6. Chapter 7 proposes a series of improvements to further optimize the whole system, while in Chapter 8 the thesis is concluded.

Chapter 2

Theory and Physics Behind PCB Design and Wireless Power Transfer

The aim of this chapter is to give the fundamentals of PCB design, with a particular attention to radiofrequency. Moreover, the wireless power transfer method will be illustrated with considerations about human safety.

2.1 Radiofrequency PCB design

Designs above 100 MHz are typically considered RF and, being very sensitive to noise and reflections, they must be treated with attention. The main issue is that the wavelength of the signal becomes comparable with the physical length of the traces and lumped models cannot be applied. In PCB design, starting from the guide wavelength λ_g (Eq. 2.1), it is possible to define a critical trace length L_g (Eq. 2.2) above which it is fundamental to pay attention to the impedance [15]. Above L_g we speak about the traces as "transmission lines", below L_g the trace can be treated as a lumped element.

$$\lambda_g = \frac{c}{f}\frac{1}{\sqrt{\epsilon_{eff}}}; \tag{2.1}$$

In the latter, c is the velocity of light, f is the frequency at which the signal will propagate through the conductor and ϵ_{eff} is the effective dielectric constant of the material between the traces.

$$L_g = \frac{\lambda_g}{16} \tag{2.2}$$

2.1.1 The importance of impedance matching

The principal cause of reflections is impedance mismatching. When designing a printed circuit board, in order to have the maximum power delivered to the load, it is important to have every load impedance (Z_L) equal to the source impedance (Z_S) and to the characteristic impedance (Z_0) of the transmission line between the two (Fig. 2.1). To avoid complications, most of the RF systems are designed around 50 Ω. In this way, PCB layouts can be more straightforward, because all the transmission lines are designed with Z_0=50 Ω [16].

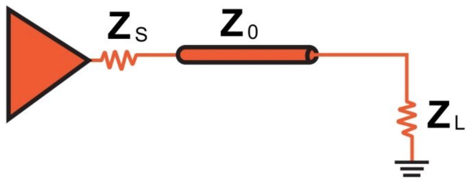

Figure 2.1: Impedance matching in RF designs. Reprinted from [16].

The quality of a match can be defined with the reflection coefficient:

$$\Gamma = \frac{Z_L - Z_S}{Z_L + Z_S} \tag{2.3}$$

If the transmission line is the source, the equation becomes the following:

$$\Gamma = \frac{Z_L - Z_0}{Z_L + Z_0} \tag{2.4}$$

The reflection coefficient has a value between zero and one. If $Z_L = Z_0$, $\Gamma = 0$ and the line impedance is perfectly matched to the load, leading to no reflection and minimizing the return loss.

2.1.2 Modelling transmission lines

A transmission line is a conductor of length Δz that is able to transport energy from one point to another. The current flowing in every conductor generates a magnetic field around them that gives raise to an inductance per unit of length $\mathcal{L}$ [H/m]. Similarly, the ohmic losses generate a resistance $\mathcal{R}$ [Ω/m] and the conductors that are close to each others create a capacitance $\mathcal{C}$ [F/m]. The dielectric that separates the conductors is also characterized by a small conductivity $\mathcal{G}$ [S/m] and must be taken into account [17]. The equivalent circuit of a transmission line is shown in Fig. 2.2.

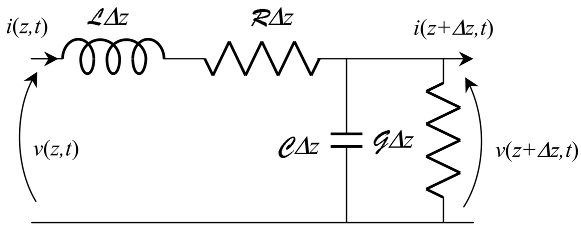

Figure 2.2: Equivalent circuit of a transmission line. Reprinted from [17].

As for every circuit, the Kirchhooff voltage and current laws (KVL, KCL) are valid (Eq. 2.5).

$$\begin{cases} v(z,t) - v(z+\Delta z,t) = \mathcal{R}\Delta z i(z,t) + \mathcal{L}\Delta z \dfrac{\partial}{\partial t} i(z,t) \\ i(z,t) - i(z+\Delta z,t) = \mathcal{G}\Delta z v(z+\Delta z,t) + \mathcal{C}\Delta z \dfrac{\partial}{\partial t} v(z+\Delta z,t) \end{cases} \tag{2.5}$$

Dividing both sides by Δz and applying the limit $\Delta z \to 0$ it is possible to obtain the transmission lines equations, also known as telegrapher's equations (Eq. 2.6).

$$\begin{cases} -\dfrac{\partial}{\partial z} v(z,t) = \mathcal{R} i(z,t) + \mathcal{L} \dfrac{\partial}{\partial t} i(z,t) \\ -\dfrac{\partial}{\partial z} i(z,t) = \mathcal{G} v(z,t) + \mathcal{C} \dfrac{\partial}{\partial t} v(z,t) \end{cases} \tag{2.6}$$

The equations are solved with the specific boundary conditions of the circuit, considering the loads and generators and the initial status at t=0. From the telegrapher's equations it is possible to derive one of the most important parameters of the model: the characteristic impedance of the transmission line Z_0 (Eq. 2.7).

$$Z_0 = \sqrt{\frac{\mathcal{R} + j\omega\mathcal{L}}{\mathcal{G} + j\omega\mathcal{C}}} \tag{2.7}$$

2.1.3 Line Types and Characteristic Impedance

As mentioned in Section 2.1.1, it is extremely important to have the characteristic impedance of the transmission line equal to the load, which is typically $50\,\Omega$. Traces can be designed with different methodologies, the most diffused are microstrips and striplines (Fig. 2.3). In addition to those, it is also possible to find coplanar and edge coupled coplanar waveguides, substrate integrated waveguides and slotlines [15]. Modulating the width and thickness of the conductor and the distance between the trace and the ground plane, it is possible to obtain $Z_0 = 50\,\Omega$.

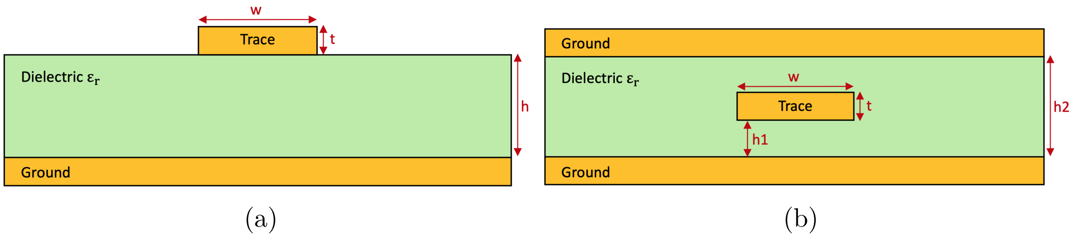

Figure 2.3: Line Types. (a) Microstrip; (b) Centered Stripline.

The signal propagation generates electromagnetic coupling between the line and the reference plane. In a microstrip, the electromagnetic field is denser in the region of dielectric between the trace and ground but there is also some field in air, therefore the propagation is quasi-TEM (transverse electromagnetic). In a stripline the field is present only in the dielectric and there is coupling with two reference planes. The propagation in a stripline is rigorously TEM.
The surface of copper, close to the substrate, is usually intentionally very rough because it increases the adhesion. Due to this roughness, the effective length of the transmission line is higher in proximity of the substrate, generating a skin effect and leading to significant losses. Striplines are typically narrower and guarantee higher shielding due to the surrounding ground planes, however microstrips, having only one surface in contact with the substrate, exhibit lower loss compared to the other geometries and are better suited for long lines. The total loss α_t (Eq. 2.8) is given by the sum of conductor losses, dielectric losses and, in a microstrip, also radiation losses, which are negligible if there is close coupling between the trace and the reference plane.

$$\alpha_t = \alpha_c + \alpha_d + \alpha_r \tag{2.8}$$

Characteristic impedance of the lines

The calculation of the impedance of a transmission line is really complex. It is possible to find a wide number of approximated formulas to derive Z_0. The IPC global association has the goal to standardize the requirements for electronics with one goal: to "build electronic better". One of the IPC standards is the IPC-2252 in which it is possible to find a design guide for RF circuits [18]. The impedance of a microstrip is described in Eq. 2.9 and it represents the simple model in which there is only one dielectric and the thickness of the conductor is null.

$$Z_{0,0,1}(u) = \frac{\eta_0}{2\pi} \ln \left[\frac{6 + (2\pi - 6) \exp \left[- \left(\frac{30.666}{u} \right)^{0.7528} \right]}{u} + \sqrt{1 + \frac{4}{u^2}} \right] \tag{2.9}$$

where η_0 is the impedance of free space ($376.73\,\Omega$) and u is the ratio between the width of the trace and the thickness of the dielectric substrate ($u = \frac{w}{h}$). Eq. 2.9 is only a model, but its accuracy is higher than 0.01% with $u < 1$ and than 0.03% for $u \leq 1000$. Moreover the model refers to a trace with negligible thickness. To consider a finite thickness, the value of u is corrected and then used in Eq. 2.9 to define a more accurate value of characteristic impedance.
For an homogeneous dielectric, u becomes u_1 as in Eq. 2.10.

$$u_1 = u + \frac{T}{\pi} \ln \left[1 + \frac{4e}{T} \tanh^2(\sqrt{6.517u}) \right] \tag{2.10}$$

where T is the ratio between the thickness of the trace and the one of the substrate ($T = \frac{t}{h}$). In a mixed dielectric u it is corrected in u_r, as in Eq. 2.11. When one dielectric is air and the other is the substrate it is said to be a mixed dielectric.

$$u_r = u + \frac{(u_1 - u)}{2} \left[1 + \frac{1}{\cosh\left(\sqrt{\varepsilon_\mathrm{r} - 1}\right)} \right] \tag{2.11}$$

To finally calculate the characteristic impedance of the microstrip considering a finite thickness and mixed dielectrics, it is necessary to derive the effective permittivity of the system (Eq. 2.12 shows the static ϵ_{eff}).

$$\varepsilon_{r,eff,dc}\left(u, \varepsilon_r\right) = \frac{\varepsilon_r + 1}{2} + \frac{\varepsilon_r - 1}{2} \left(1 + \frac{10}{u_r} \right)^{-a_\mu b_\varepsilon} \tag{2.12}$$

where a_μ and b_ϵ are reported in Appendix A.1. The static characteristic impedance of a microstrip with finite thickness and mixed dielectrics is given in Eq. 2.13.

$$Z_0\left(u,\ T, \varepsilon_r\right) = Z_{0,0,1}(u) \frac{1}{\sqrt{\varepsilon_{r,eff,dc}\left(u, \varepsilon_r\right)}} \tag{2.13}$$

Since the characteristic impedance varies only slightly with the frequency [19] and can be neglected, the frequency dependant equations are not reported here but can be found in [18].

For striplines, the value of Z_0 is computed with different equations for either narrow ($\frac{w}{h_2-t} \leq 0.35$, Eq. 2.14) or wide ($\frac{w}{h_2-t} > 0.35$, Eq. 2.15) lines.
The characteristic impedance of a narrow line is:

$$Z_0 = \frac{60}{\sqrt{\varepsilon_r}} \ln \left(\frac{4\ h_2}{\pi w \frac{1}{2} \left[1 + \left(\frac{X}{\pi}\right)\right] \left[1 + \ell n \left(\frac{4\pi}{X}\right) + 0.51\pi X^2\right]} \right) \tag{2.14}$$

where $X = \frac{t}{w}$.
The characteristic impedance of a wide line is give by:

$$\mathrm{Z}_0 = \frac{94.15}{\sqrt{\varepsilon_r \left(\frac{[2\chi \ell n(\chi + 1) - (\chi - 1)\ell n\,(\chi^2 - 1)]}{\pi} + \frac{w}{h_2 - t} \right)}} \tag{2.15}$$

with $\chi = \frac{h_2}{h_2-t}$.

In Fig. 2.4 it is possible to appreciate how the geometry influences the impedance of a trace [20].

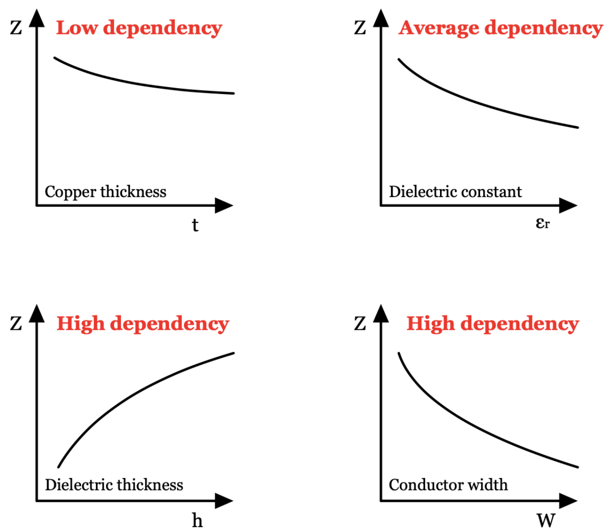

Figure 2.4: Influence of geometry on the characteristic impedance of PCB traces.

2.2 Wireless Power Transfer to Freestanding Electrodes

The first designs of clinical neural prostheses were done following the first implantable battery-powered pacemaker: a microelectrodes array connected to an implantable electronic unit (IEU) with cables that were either signal processors for neural recording or implantable pulse generators (IPG) for neurons stimulation. Modern designs are moving toward a completely wireless stimulation with arrays of freestanding electrodes because cables and IEUs often lead to complications: damage of tissues due to mechanical forces, infections, heat generation and risk of failure due to the leakage in a wet environment. The greatest challenge of designing a truly wireless system of free-floating implants is to be able to deliver sufficient power to the electrodes while miniaturizing the implants [21].

2.2.1 Overview of the Techniques

Wireless power transfer (WPT) systems for miniaturized implants can be described by three indicators: efficiency of the link, penetration depth and size of the receiver. In Fig. 2.5, five methodologies are compared: acoustic power transfer (APT), inductive power transfer (IPT) and capacitive power transfer (CPT) in near-field, RF radiation in mid-field and far-field. The most suitable methodologies for miniaturized implants are IPT, CPT and APT [22].

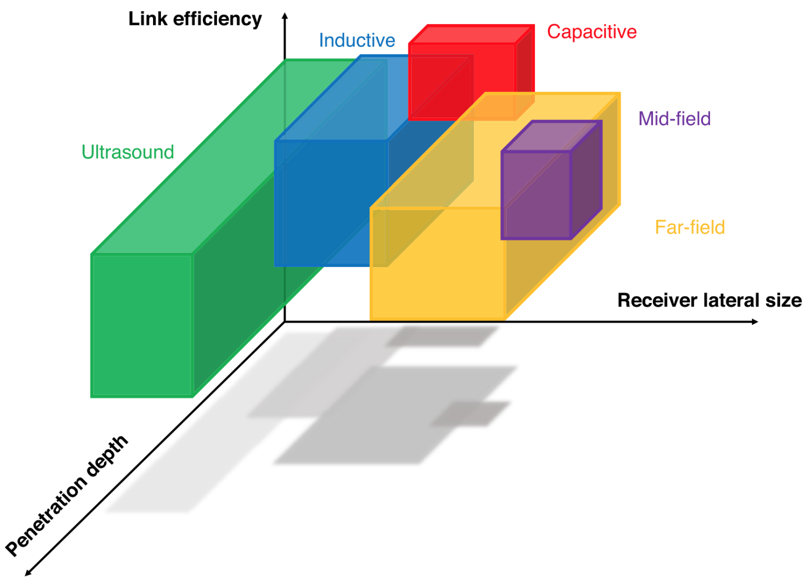

Figure 2.5: Comparison of the WTP techniques. Reprinted from [22].

The three techniques show advantages and weaknesses and their use strongly depends on the desired application.
APT allows high penetration depth and high input power but its fabrication is challenging since it usually requires other components bonded with a PCB, thus increasing the size of the implant. CPT systems are less affected by rotation and misalignment but the frequency needs to be increased to have an efficient power transfer. The latter disadvantage is true also for IPT, but can be overcome with the use of 3-coils structures which increase the efficiency and reduce the problem of misalignment. CPT and IPT are the best choices for multiple implants. Capacitive systems are more suitable for larger receivers at short distance while inductive ones are the best for intermediate depths and smaller implants allowing high resolution intra-cortical stimulation.

2.2.2 Inductive Power Transfer

IPT is the most used WPT method and has been largely investigated over the years. The inductive methodology is appreciated in the medical field because it relies on RF in the near-field which is less attenuated by the tissues. IPT has gained a lot of interest also for other applications: near-field radio-frequency identification (RFID) for transponders and mobile and vehicles charging [23]. When designing an IPT system, a high-efficiency power amplifier is typically placed at the side of the transmitter (Tx) connected to primary coil that is mutually coupled to the secondary coil at the side of the receiver (Rx), which is connected to a certain load (R_L). The mutual inductance (M_{ij}) between coupled coils is proportional to d^{-3} where d is the spacing between the center of the coils. The fundamental requirement of the IPT link is to have the sufficient power delivered to the load (PDL) with high power transfer efficiency (PTE) to avoid the dissipation of heat in the tissues. Many parameters influence the PDL and PTE, such as the geometry of the coil, the distance and the alignment. Besides the conventional 2-coil link, other configurations that have been studied were found to be very promising [24]: the 3-coil and the 4-coil IPT. The 3-coil method provides a PTE as large as the 4-coil one but it guarantees a PDL that is remarkably higher respect to the other techniques at large d [25]. In Fig. 2.6, a comparison between the 3-coil and 4-coil inductive links highlights the fact that, with a 3-coil system, it is possible to achieve simultaneously high PTE and high PDL. The comparison is done considering the distance d between the coils and their coupling coefficient (Eq. 2.16).

$$k_{ij} = \frac{M_{ij}}{\sqrt{L_i L_j}} \tag{2.16}$$

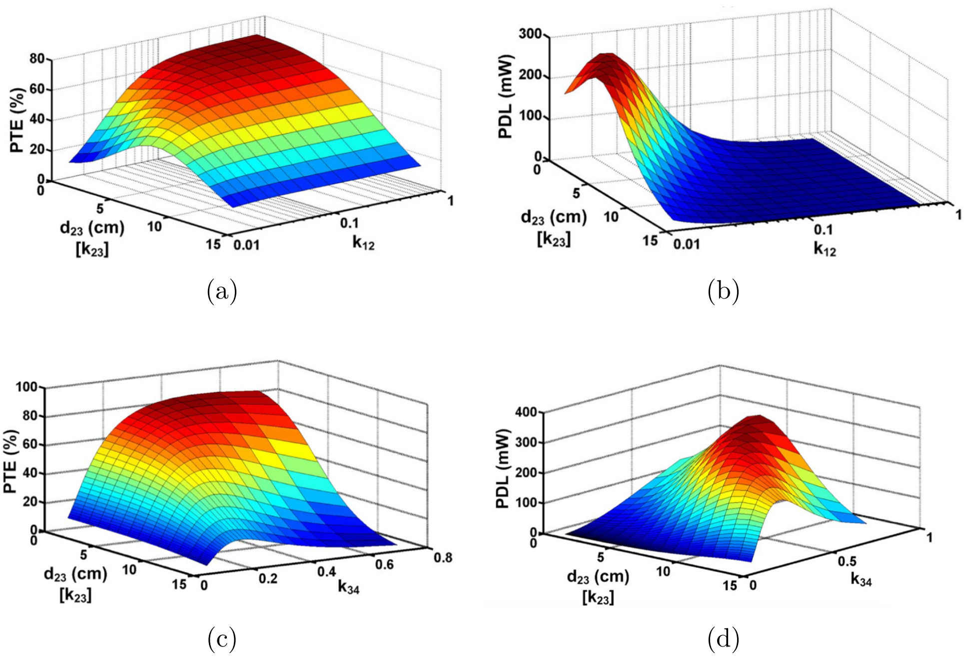

Figure 2.6: Comparison of PTE and PDL vs. distance d_{ij} and coupling coefficient k_{ij} in 3-coil and 4-coil IPT. (a) PTE and (b) PDL for a 4-coil IPT; (c) PTE and (d) PDL for 3-coil IPT. Reprinted from [25].

In every system, the largest PTE is achieved if all the LC tanks resonate at the same frequency $f_0 = 1/2\pi\sqrt{LC}$ [26] and, at resonance, it is possible to determine what is the reflected impedance that the receiver generates toward the transmitter. The operating and resonating frequency can be changed with the correct value of capacitance, placed serially or in parallel to the coil.

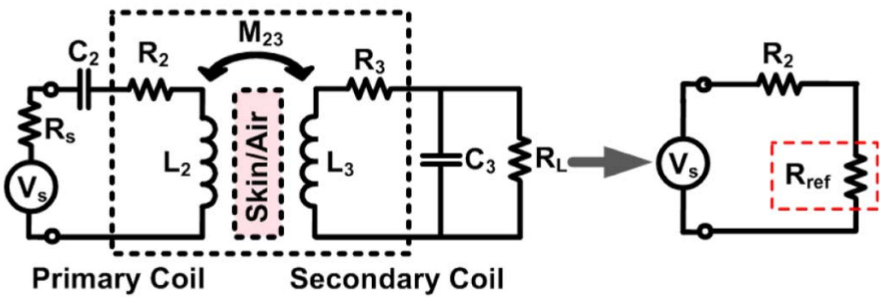

Figure 2.7: Model of a 2-coil IPT with equivalent circuit obtained from the reflected load at resonant frequency. Reprinted from [25].

For a 2-coil system (Fig. 2.7), the reflected impedance is calculated as follows:

$$R_{ref} = k_{23}^2 \omega_0 L_2 Q_{3L} = k_{23}^2 R_2 Q_2 Q_{3L} \tag{2.17}$$

where k_{23} is the coupling coefficient defined in Eq. 2.16 and Q is the quality factor: $Q_2 = \omega_0 L_2/R_2$ and $Q_{3L} = Q_3 Q_L/(Q_3 + Q_L)$ with $Q_3 = \omega_0 L_3/R_3$ and the load quality factor $Q_L = R_L/\omega_0 L_3$.
The quality factor of a coil is one of the most important parameters because it estimates the capacity of the coil to generate the magnetic field and its ability to transfer power. Another way to calculate Q is to use Eq. 2.18, where Z is the frequency-dependent impedance of coil. This method is used when it is possible to obtain the scattering matrix of the coil, either from simulations or measurements with a network analyzer.

$$Q = \frac{Im(Z)}{Re(Z)} \tag{2.18}$$

When a receiver is powered by a transmitter, the output power of the source divides between R_2 (which includes also the source impedance R_s) and R_{ref} and divides again between R_L and R_3. The efficiency of a 2-coil IPT is given by η.

$$\eta_{2-\text{coil}} = \frac{k_{23}^2 Q_2 Q_{3L}}{1 + k_{23}^2 Q_2 Q_{3L}} \cdot \frac{Q_{3L}}{Q_L} \tag{2.19}$$

The power delivered to the load is:

$$P_{L,2-\text{coil}} = \frac{V_s^2}{2R_2} \frac{k_{23}^2 Q_2 Q_{3L}}{(1 + k_{23}^2 Q_2 Q_{3L})^2} \cdot \frac{Q_{3L}}{Q_L} \tag{2.20}$$

The 2-coil system is the simplest case and the equations can be extended for any m-coil inductive link. The reflected load from the (j+1)th coil to the previous one is given in Eq 2.21.

$$R_{\text{ref } j,j+1} = k_{j,j+1}^2 \omega_0 L_j Q_{(j+1)L} \qquad j = 1,2,\ldots,m-1 \tag{2.21}$$

Where $Q_{(j+1)L}$ is obtained from:

$$Q_{jL} = \frac{\omega_0 L_j}{R_j + R_{\text{ref } j,j+1}} = \frac{Q_j}{1 + k_{j,j+1}^2 Q_j Q_{(j+1)L}} \qquad j = 1,2,\ldots,m-1 \tag{2.22}$$

In the latter equation $Q_j = \omega_0 L_j/R_j$ represents the unloaded quality factor. Considering only the coupling between neighbour coils, the total PTE is found from:

$$\eta_{m-\text{coil}} = \prod_{j=1}^{m-1} \eta_{j,j+1} \cdot \frac{Q_{mL}}{Q_L} \tag{2.23}$$

while the PDL is:

$$P_{L,m-\text{coil}} = \frac{V_s^2}{2R_1}\frac{1}{1+k_{12}^2 Q_1 Q_{2L}}\eta_{m-\text{coil}} \tag{2.24}$$

In any inductive link it is possible to define the values of optimal load for both the PTE ($R_{L,PTE}$) and the PDL ($R_{L,PTE}$), in particular the PDL is maximised if R_{ref} matches the primary coil impedance, even if in this situation the PTE will be always lower than 50% because the power is split between the two impedances.

3-Coil IPT link

When designing an IPT link, one of the most difficult challenges is to achieve sufficient PDL and adding a resonator close to the Rx plane can be very useful for this purpose [21]. In particular, it was found that a high Q resonator improves both the PDL and the PTE due to the boosting of the magnetic field and because it distributes homogeneously the power over the area of the receivers. Achieving a high value of Q with the resonator is not straightforward because the presence of tissues highly reduces the quality factor. Moreover, being implanted in the body, the resonator must be encapsulated in a biocompatible material which also influences Q.

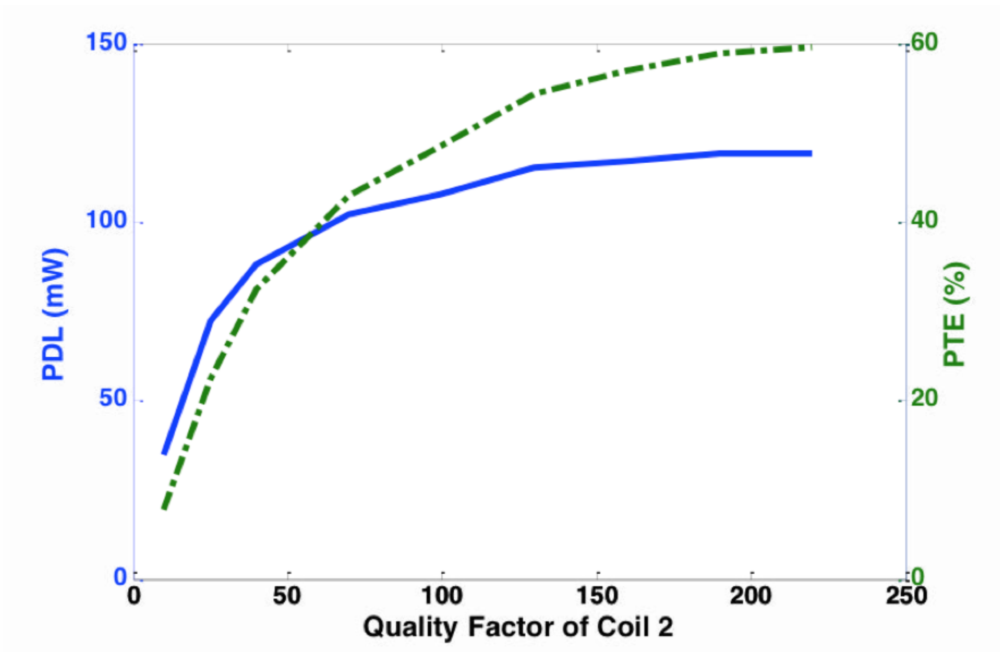

Figure 2.8: PTE and PDL as function of the resonator quality factor. Reprinted from [24].

The great advantage of the 3-coil IPT link is the fact that the additional loop can function as an impedance-matching circuit and it is possible to convert any R_L in the desired reflected impedance, for instance to obtain R_{ref} equal to R_2 and maximise the PDL.

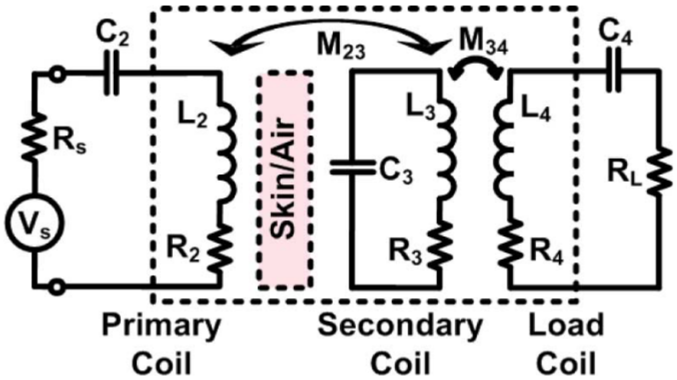

Figure 2.9: 3-coil inductive link. Reprinted from [25].

The efficiency of the 3-coil link is derived in Eq. 2.25, where the coupling between the primary and the third loop is neglected.

$$\eta_{3-\text{ coil}} = \frac{\left(k_{23}^2 Q_2 Q_3\right)\left(k_{34}^2 Q_3 Q_{4L}\right)}{\left[\left(1+k_{23}^2 Q_2 Q_3+k_{34}^2 Q_3 Q_{4L}\right)\left(1+k_{34}^2 Q_3 Q_{4L}\right)\right]} \cdot \frac{Q_{4L}}{Q_L} = \eta_{23}\eta_{34} \tag{2.25}$$

The power deliver to the load is:

$$P_{L,3-\text{ coil}} = \frac{V_s^2}{2R_2} \frac{\left(k_{23}^2 Q_2 Q_3\right)\left(k_{34}^2 Q_3 Q_{4L}\right)}{\left(1+k_{23}^2 Q_2 Q_3+k_{34}^2 Q_3 Q_{4L}\right)^2} \cdot \frac{Q_{4L}}{Q_L} \tag{2.26}$$

Moreover, the presence of the resonator allows to energetically cover a wider region than the 2-coil system [27]. In Fig. 2.10, the 2-coil IPT is compared with the 3-coil one, in terms of Poynting vector. The red area in the figure shows where the power density reaches its maximum value, in this case $10\,\mathrm{W/m^2}$, and it is possible to appreciate the fact that the area inside and also slightly outside of the resonator receives a high and homogeneous amount of power. With this homogeneous distribution, also the impact of misalignment and angular rotation is reduced [28], being a great advantage for brain applications since the brain is not flat.

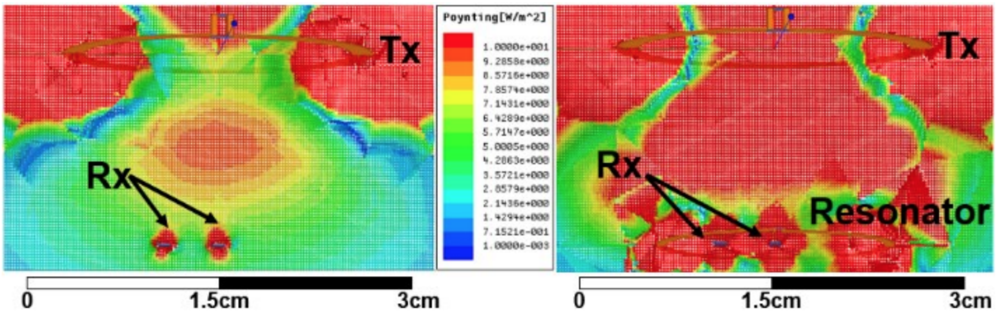

Figure 2.10: Comparison of power density distribution between 2-coil IPT (left) and 3-coil IPT (right). Reprinted from [27].

S-Parameters and Measurement Systems

In order to know and describe in the most accurate way the parameters of a single coil or an inductive link, the best approach is to discover the scattering parameters. From the S-matrix, it is possible to obtain the real and imaginary parts of the impedance of the coils and from those values it is easy to derive other parameters such as the inductance or the quality factor. The S-parameters can be obtained in simulations software as Ansys HFSS, or connecting the coils to a Network Analyzer.

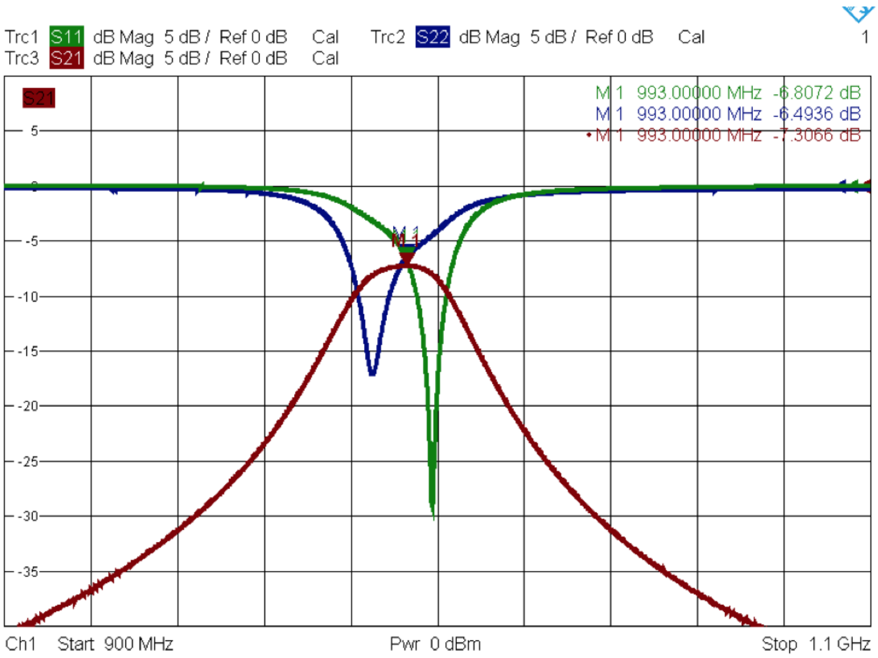

Figure 2.11: S-parameters of an inductive link. Reprinted from [29]

When considering a single coil, the most important parameter is the return loss: S11. The return loss indicates the ratio between the amount of reflected power and the amount of the incident power at a certain frequency. At the operating frequency, the value of S11 should be minimized to assure that no power will be reflected backward. The minimum peak of the S11 curve is shifted by placing a capacitor in series or parallel to the loop. When considering the link between two coils, besides considering the return loss on the single ones, the forward transmission S21 should be at maximum. From Fig 2.11 it is possible to see that in an inductive link, where the return loss of the coils is minimized, the forward transmission is high. As mentioned already, the IPT technology is usually characterized by using a Network Analyzer, while the PDL can be tested with a Spectrum Analyzer. However, it must be considered that the instruments that are used for the measurements typically have only 50 Ω ports, while the actual source and load resistance of the whole system might be different. A measurement method to overcome this issues is to place additional resistances in the setup [30]. If the load or source resistance is higher than 50 Ω, a resistance must be added in series with the port of the Analyzer, if the resistance is lower than 50 Ω, the additional resistance must be added in parallel. A visual explication of the setup measurement is shown in Fig. 2.12.

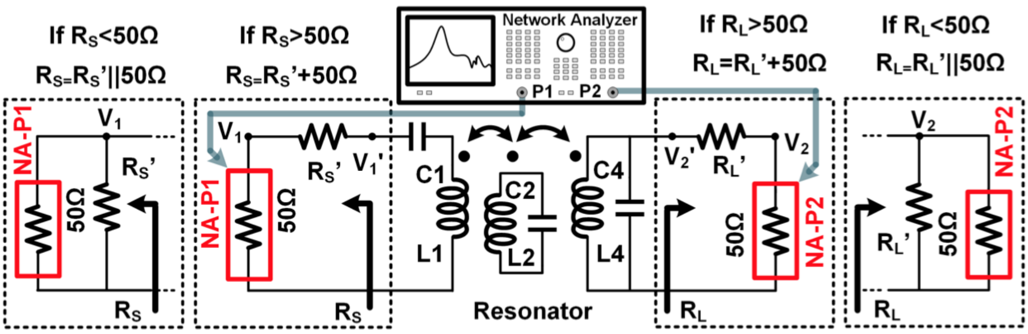

Figure 2.12: System measurement with Network Analyzer adapting the source and load impedances. Reprinted from [30].

Self Resonance Frequency of a Coil

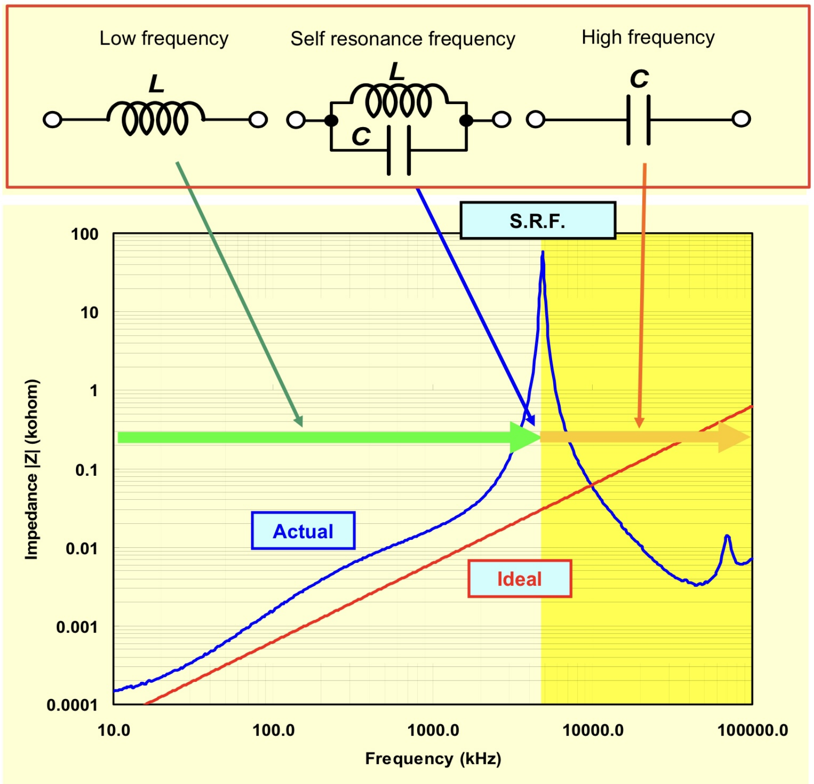

Figure 2.13: Impedance of the coil vs. frequency. Reprinted from [31].

When designing an inductive link, one of the first parameters that must be considered is the self resonance frequency (SRF) of the coil, which differs from the resonance frequency of the LC tank. The SRF is originated from the parasitic capacitances of the coil that are due to the traces of the coil being close to each others [32]. To avoid the effect of the parasitic capacitances, a general law is to have the operating frequency $f_0 < 10 \cdot f_{SRF}$. SRF depends on the design of the coil. The inductance is increased with the number of turn, but the SRF decreases due to the higher resistance and parasitic capacitance, while a large width of the traces increases the quality factor but it also reduces the SRF. If the operating frequency must be high, it is preferable to have one or few turns or narrower traces even if the the inductance will be reduced [33]. The impedance of an ideal coil is $Z = j2\pi f L$, increasing linearly with frequency. In reality, the coil can be modeled as an inductor in parallel with a capacitor and the impedance becomes $Z(s) = \frac{sL}{1+s^2LC}$ [31]. From the latter equation, it is evident that the Bode function presents a double pole in correspondence of

$$f_{SRF} = \frac{1}{2\pi\sqrt{LC}} \tag{2.27}$$

where the impedance does not increase linearly with the frequency but it reaches a maximum value and starts to decrease (Fig. 2.13).
In correspondence of the SRF, the phase angle of the impedance is zero and, consequently, Q is zero, as well as the effective inductance, and the S21 is at minimum [34].

2.2.3 Specific Absorption Rate and ISM Bands

When the human body is exposed to RF, the energy absorbed by the tissues can become dangerous. The Federal Communication Commission has decided that the Specific Absorption Rate (SAR) must not overcome the value of 1.6 W/kg for 1 g of tissue in 6 minutes of exposure in the human brain [35]. The definition of SAR is:

$$SAR = \frac{\sigma |E_{rms}|^2}{\rho} \tag{2.28}$$

where σ defines the tissue conductivity and ρ the density, while E_{rms} is the round value of the electric field. From the Maxwell's equation (Eq. 2.29) it is possible to understand the trend of the SAR which is proportional to $(\omega_0 I)^2$ (with ω_0 the operating frequency and I the current flowing in the coil) [36][1].

$$\nabla \times E = -\frac{\partial B}{\partial t} \propto \omega_0 I \tag{2.29}$$

The frequency of operation must be chosen accordingly to the ISM radio bands that are reserved for industrial, scientific and medical purposes and not for telecommunications [37][38]. The available bands are described in Tab. 2.1 [39].

ISM Band Frequencies
6.765 MHz to 6.795 MHz
13.553 MHz to 13.567 MHz
26.957 MHz to 27.283 MHz
40.66 MHz to 40.70 MHz
83.996 MHz to 84.004 MHz
167.992 MHz to 168.008 MHz
433.05 MHz to 434.79 MHz
886 MHz to 906 MHz
2.4 GHz to 2.5 GHz
5.725 GHz to 5.875 GHz
24.0 GHz to 25.25 GHz
61.0 GHz to 61.5 GHz
122 GHz to 123 GHz
244 GHz to 246 GHz

Table 2.1: Bands reserved for industrial, scientific and medical (ISM) purposes.

From a study done for the ENGINI's project [40], where the acronym stands for: Empowering Next Generation Implantable Neural Interface; it was found that the 433.92 MHz ISM band can deliver the highest power while respecting the limit of SAR (1.6 W/kg).

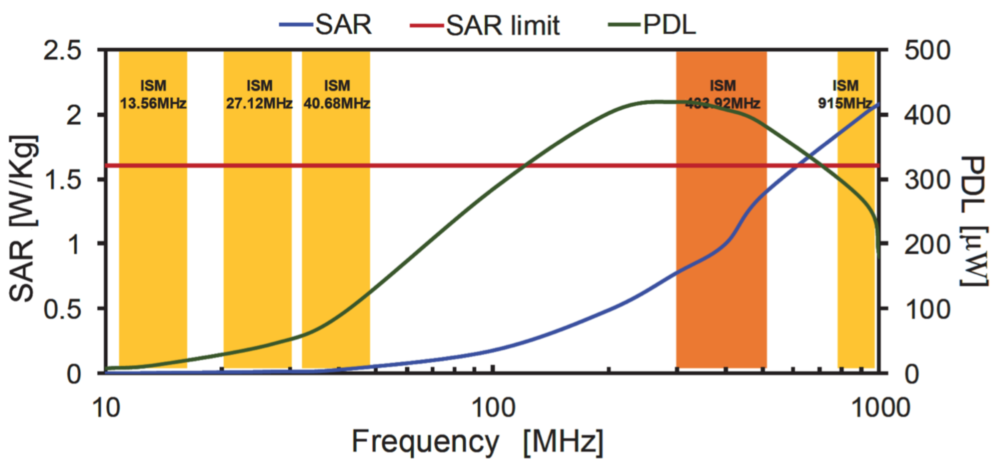

Figure 2.14: PDL and SAR for the ISM bands. Reprinted from [40].

Chapter 3

RF SWIPT Base Station Design

The aim of the base station is to generate a wave in the band of 433.92 MHz, and modulate it accordingly to the digital input received from the image processing. The signal is then amplified to increase the power delivered to the implanted receivers. In this chapter, the initial architecture for the RF SWIPT base station designed by Barbruni *et al.* is presented. Subsequently, all the modifications and improvements of the blocks for PCB integration are explained, together with the design strategies.

3.1 System Architecture

The system is made of four main blocks and a transmitting coil (Fig. 3.1).

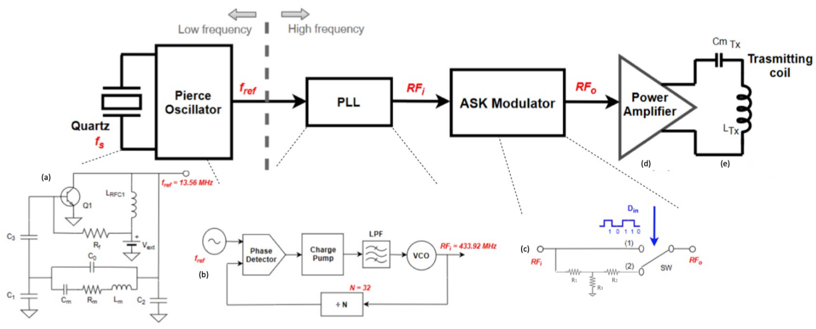

Figure 3.1: System architecture: a) Pierce Oscillator; b) Phase-Locked Loop; c) Amplitude-Shift Keying Modulator; d) Power Amplifier; e) Transmitting Coil. Reprinted from [1] and modified.

- **Pierce Oscillator**: Designed with a crystal quartz to obtain an initial wave at 13.56 MHz;
- **Phase-Locked Loop (PLL)**: To multiply the frequency of the wave by 32 and reach the 433.92 MHz band;
- **Amplitude-Shift Keying (ASK) Modulator**: To modulate the amplitude of the wave and distinguish the digital bits for information delivery;
- **Power Amplifier (PA)**: To increase the power delivered to load.

3.2 New design of the blocks for PCB integration

All the blocks have been improved and modified to allow the integration of the whole circuit in a PCB and to optimize the design for the needed frequency. A microcontroller was added to set correctly the registers of the PLL.

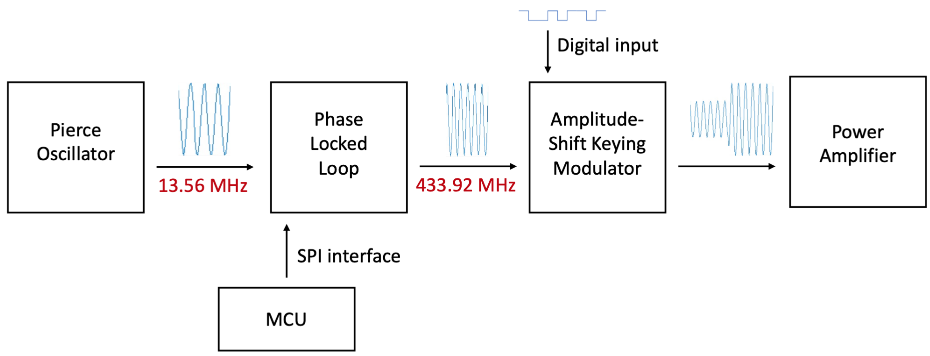

Figure 3.2: RF SWIPT Station for PCB Design

3.2.1 Pierce Oscillator

The first block of the PCB is a low frequency Pierce oscillator used to generate the initial wave at 13.56 MHz. The oscillator is built with a quartz crystal with optimal stability to guarantee a perfect oscillation since, after the multiplication of the frequency with the PLL, the signal has to fit in a very narrow ISM band: [433.05 ÷ 434.79] MHz. The quartz that was initially used for breadboard is the

AT-51, manufactured by NDK. Unfortunately the quartz is no more present on the market, and it was necessary to select a new one and slightly modify the design of the Pierce oscillator, considering also the parasitic capacitances of the PCB. The crystal chosen for the block is the surface-mount NX5032GA [41], also manufactured by NDK. The parameters of the crystal are reported in Tab. 3.1.

C_0	C_m	L_m	ESR	C_L
3.10 fF	0.94 pF	44.8 mH	120 Ω	8 pF

Table 3.1: NX5032GA parameters.

When re-designing the Pierce, two main factors must be considered:

- The load capacitance of the crystal has changed. In AT-51 the load capacitance was 16 pF, while in NX5032GA it is 8 pF.
- In a PCB, it is necessary to take into account its stray capacitance, which is typically between 3 pF to 7 pF.

The change that is needed is the value of the external capacitors that are placed between the terminals of the quartz crystal and the reference plane. In order to have the correct frequency of oscillation, Eq. 3.1 must be satisfied.

$$C_L = \frac{C_a \cdot C_b}{C_a + C_b} + C_{stray} \tag{3.1}$$

C_a and C_b are typically chosen to be equal, considering that $C_L = 8\,pF$, the total capacitance from one terminal of the quartz to reference must be equal to 8 pF as well. Considering the range of C_{stray}, it is quite straightforward that the value of the external capacitances must be very low, or even null. One way to deal with this unknown C_{stray}, is to place in the PCB design two footprints to eventually insert a proper capacitor later if the quartz does not oscillate properly. The oscillation was verified simulating the Pierce on LTSpice considering 8 pF as a reasonable value for the stray capacitance.

3.2.2 Phase-Locked Loop

The Phase-Locked Loop is inserted in the architecture to achieve a frequency in the band of 433.92 MHz. The PLL used for this block is the LTC6948-1 by Analog Devices [42]. Starting from an oscillation of 13.56 MHz, the registers of the PLL must be set to multiply the frequency by 32. In the initial architecture realized with the demo boards, every time the system was powered up, the PLL needed

to be programmed with another PCB, the Linduino DC2026C by Analog Devices, that had to be attached to the computer. Considering the final application (the PCB placed over the patient's head), this is not acceptable. The communication between the two boards is done with the SPI protocol, that will be explained in details in Section 3.3, and the demo board of the PLL has a complex SPI interface to recognize the programming board. To avoid the use of this supplementary board, a microcontroller was inserted in the system and programmed to fill the registers of the PLL by using its SPI interface.
The registers of the PLL are fifteen, thirteen of them must be written with the correct information to set the output.
The registers are described in the table of Fig. 3.3.

ADDR	MSB	[6]	[5]	[4]	[3]	[2]	[1]	LSB	R/W	DEFAULT
h00	*	*	UNLOCK	ALCHI	ALCLO	LOCK	THI	TLO	R	
h01	*	*	x[5]	x[4]	x[3]	x[2]	x[1]	x[0]	R/W	h04
h02	PDALL	PDPLL	PDVCO	PDOUT	PDFN	MTCAL	OMUTE	POR	R/W	h06
h03	ALCEN	ALCMON	ALCCAL	ALCULOK	AUTOCAL	AUTORST	DITHEN	INTN	R/W	h3E
h04	BD[3]	BD[2]	BD[1]	BD[0]	CPLE	LDOEN	LDOV[1]	LDOV[0]	R/W	h47
h05	SEED[7]	SEED[6]	SEED[5]	SEED[4]	SEED[3]	SEED[2]	SEED[1]	SEED[0]	R/W	h11
h06	RD[4]	RD[3]	RD[2]	RD[1]	RD[0]	*	ND[9]	ND[8]	R/W	h08
h07	ND[7]	ND[6]	ND[5]	ND[4]	ND[3]	ND[2]	ND[1]	ND[0]	R/W	hFA
h08	*	*	NUM[17]	NUM[16]	NUM[15]	NUM[14]	NUM[13]	NUM[12]	R/W	h3F
h09	NUM[11]	NUM[10]	NUM[9]	NUM[8]	NUM[7]	NUM[6]	NUM[5]	NUM[4]	R/W	hFF
h0A	NUM[3]	NUM[2]	NUM[1]	NUM[0]	*	*	RSTFN	CAL	R/W	hF0
h0B	BST	FILT[1]	FILT[0]	RFO[1]	RFO[0]	OD[2]	OD[1]	OD[0]	R/W	hF9
h0C	LKWIN[2]	LKWIN[1]	LKWIN[0]	LKCT[1]	LKCT[0]	CP[2]	CP[1]	CP[0]	R/W	h4F
h0D	CPCHI	CPCLO	CPMID	CPINV	CPWIDE	CPRST	CPUP	CPDN	R/W	hE4
h0E	REV[3]	REV[2]	REV[1]	REV[0]	PART[3]	PART[2]	PART[1]	PART[0]	R	hxx†

*unused †varies depending on version

Figure 3.3: LTC6948-1 registers.

Address h00 and h0E can be only set in read mode, while the others can be either in read or write mode.
The output power of the PLL is fixed and can be set by filling the registers. The maximum single-ended output is 1.5 dBm and it is set with RFO[1:0]=3.
Concerning the output frequency, the multiplication by 32 is done setting the 10-bit N divider ND[9:0] that provides the feedback from the voltage-controlled oscillator (VCO) to the phase frequency detector (PFD) of the PLL. The ND[9:0] is set to 192 in order to have, from the VCO an output of $192 \cdot 13.56\,\text{MHz}$ reaching 2.60 GHz which is included in the VCO range of the LTC6948-1 (2.24 GHz to 3.74 GHz). The frequency is then divided by O_DIV[2:0] set to 6 to have $2.60\,\text{GHz}/6 = 433.92\,\text{MHz}$. The PLL block diagram is reported in Fig. 3.4 to better understand what can determined through the registers.

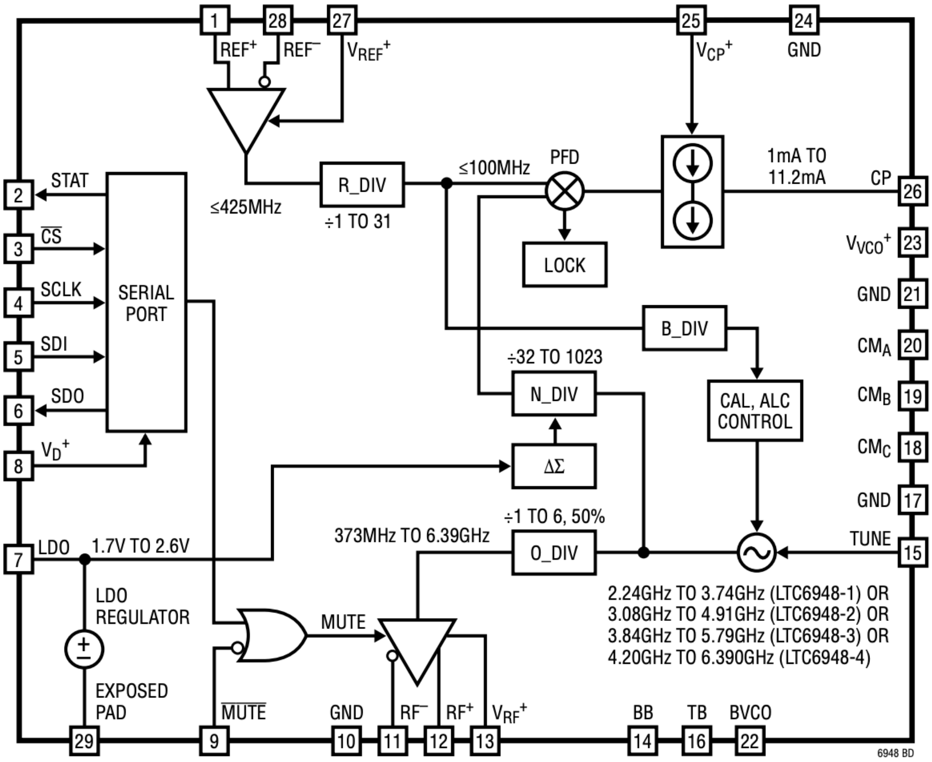

Figure 3.4: LTC6948-1 Block Diagram.

3.2.3 Amplitude-Shift Keying Modulator

The ASK modulator is composed by the M3SW-2-50DRA+ switch [43], manufactured by Minicircuits. The switch is made of one RF input and two RF outputs and it is controlled by a digital external input. One of the two outputs is then attenuated to distinguish the digital "1" from the digital "0". The presence of this block is fundamental: with the ASK modulation, the receiver will be able to distinguish the digital signals provided by the image processing, still receiving power because the amplitude of the signal is never null.
In the initial prototype of the base station, the signal was simply attenuated with an 3dB attenuator placed at the end of the SMA (SubMiniature version A) cable, but in the PCB this is not possibile and one solution is to have one of the two output lines of the switch followed by a T-Pad attenuator.

The values of resistances for the T-Pad attenuator were calculated according to Eq. 3.2. [44].

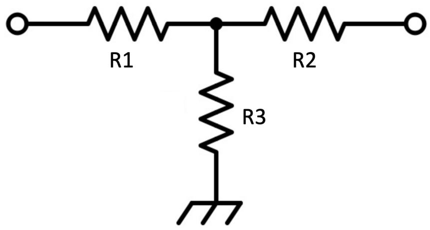

$$R_1 = R_2 = Z \cdot \frac{K-1}{K+1}$$
$$R_3 = 2Z \cdot \frac{K}{K^2-1} \tag{3.2}$$

Z is the source or load impedance, while K is the impedance factor referred to the voltages, described in Eq. 3.3.

$$K = 10^{\frac{dB}{20}} \tag{3.3}$$

To have an attenuation of 3.5 dB, K is equal to 1.496, and the values of resistance can be easily derived: R_1=R_2=9.93 Ω and R_3=120.84 Ω.
A T-Pad attenuator with the closest commercialized values of the resistance was then verified with LTspice, to assure the correct attenuation (Fig. 3.5, 3.6). The simulated input signal is the maximum that the PLL can generate: 1.5 dBm.

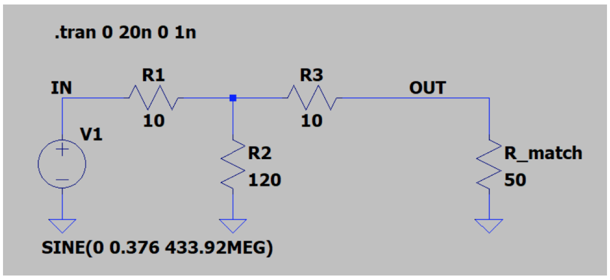

Figure 3.5: LTspice design of the T-Pad attenuator.

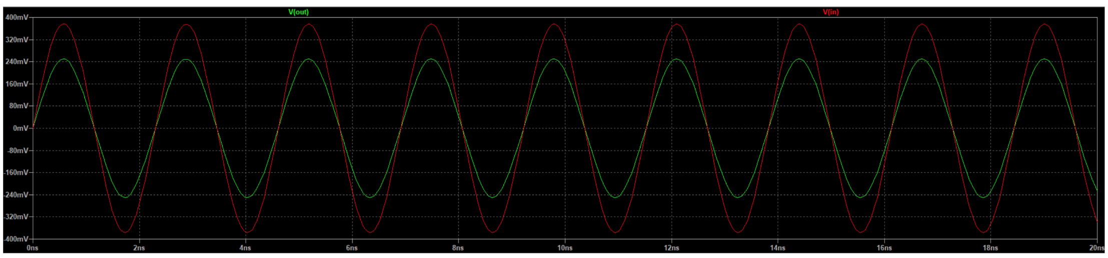

Figure 3.6: Simulation of T-Pad attenuator. Red signal before T-Pad, green signal after T-Pad.

From the simulation, it is possible to compare the input and output values of the attenuator as described in Tab. 3.2.

	IN	**OUT**
$\mathbf{V_{pp}}$	752 mV	499 mV
dBm (Z=50 Ω)	1.5	-2

Table 3.2: Input and output values of the T-Pad attenuator, extracted from LTspice simulation.

From the extracted values, it can be confirmed that the attenuation is 3.5 dB and, using the peak-to-peak voltage values, it is possible to derive the modulation index of the ASK (Eq. 3.4) [45].

$$M = \frac{V_{pp(in)} - V_{pp(out)}}{V_{pp(in)} + V_{pp(out)}} = \frac{752\,\mathrm{mV} - 499\,\mathrm{mV}}{752\,\mathrm{mV} + 499\,\mathrm{mV}} = 20\% \tag{3.4}$$

3.2.4 Power Amplifier

The power amplifier that is used to enforce the robustness of the system is a class-AB PA: RF5110G by Qorvo [46]. In the initial prototype [1], the evaluation kit was tuned for 900 MHz and it was not possible to reach the highest gain with an input signal of 433.92 MHz. To have the maximum gain and efficiency, the circuitry has been modified according to the datasheet to tune the PA at 450 MHz. The typical electrical specifications of the 450 MHz Power Amplifier are described in Tab. 3.3.

Parameter	**Typical Value**
Output Power	32 dBm
Gain	32.5 dB
Efficiency	50.%

Table 3.3: Electrical Specification of the RF5110G Power Amplifier tuned at 450 MHz.

The changes that were applied to the schematic to tune it for 450 MHz instead of 900 MHz are reported in Fig. 3.7.

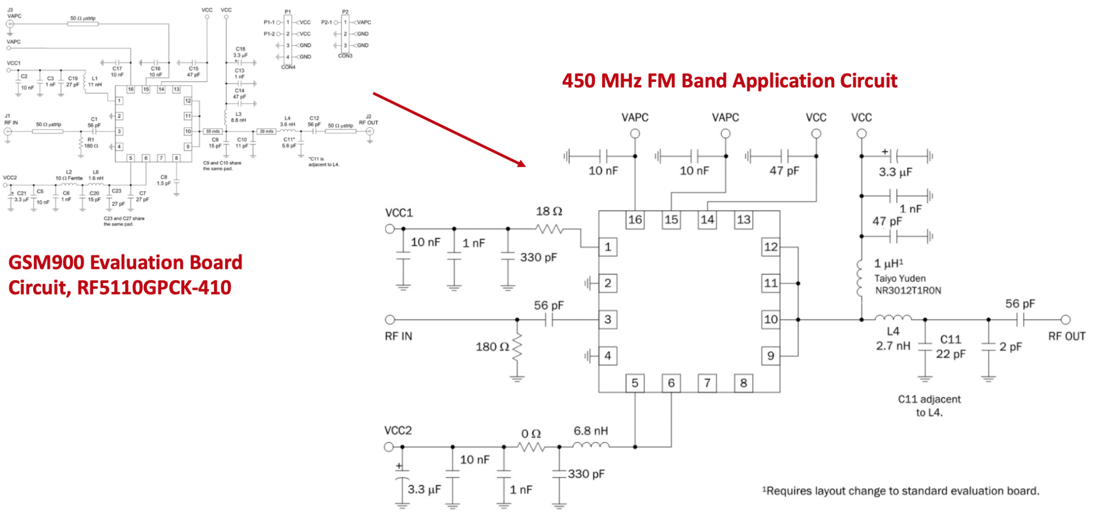

Figure 3.7: Modified schematic of the power amplifier for 450 MHz band application.

3.3 Microcontroller to set PLL

In order to have the whole RF SWIPT Base Station in only one board without the need of any additional board or software, the microcontroller MSP430G2553 by Texas Instrument was added to the PCB and programmed to send the SPI signals needed to set the registers of the PLL. A brief introduction and explanation of the SPI protocol will be given before entering in the details of the MCU programming for the special purpose.

3.3.1 SPI Protocol

The serial peripheral interface (SPI) is one of the most used communication protocols in PCBs. SPI was developed by Motorola in 1979 with the intend to link, with four wires, the microcontroller peripherals. The full duplex SPI communication is characterized by a master-slave architecture with one single master and one or multiple slaves as shown in figure 3.8.

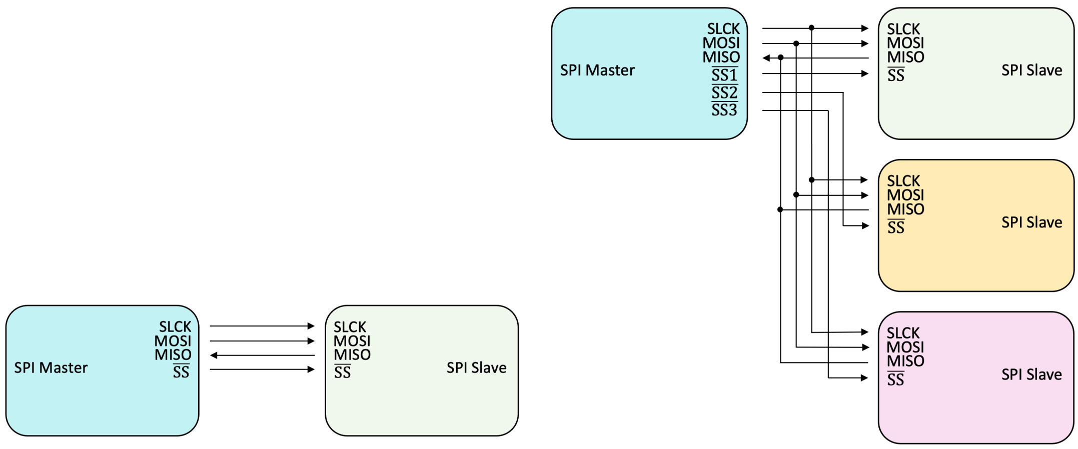

(a) (b)

Figure 3.8: SPI master-slave architecture: (a) Single slave SPI; (b) Multiple slaves SPI.

The SPI protocol is based on four digital signals:

- SCLK: Clock signal sent from the master to the slaves to allow a synchronous communication;
- MOSI: Data line sent from the master (Master Output Slave Input);
- MISO: Data line sent from the slave (Master Input Slave Output);
- $\overline{\text{SS}}$: To indicate that the data is being sent from the master and, in case of multiple slaves, to select the correct one (Slave Select).

During the communication, the master selects a slave pulling down the corresponding $\overline{\text{SS}}$ line and activates the clock that will be used by both master and slave.
The possible communication modes are four and they are defined by the clock phase (CPHA) and the clock polarity (CPOL). The master and the slave must have the same parameters and, if the master is linked to different slaves with different parameters, it needs to be reconfigured every time it has to communicate with another slave.
When there is no data transmission, the clock is pulled low if the clock polarity is 0 and high if the clock polarity is 1. The sampling edge is defined by the clock phase which is 0 if the data is sampled on the leading (first) edge and 1 if it is sampled on the trailing (second) edge.

In Fig. 3.9 it is possible to observe the different modes of operation and a representation of the four signals sent during SPI communication in mode 0.

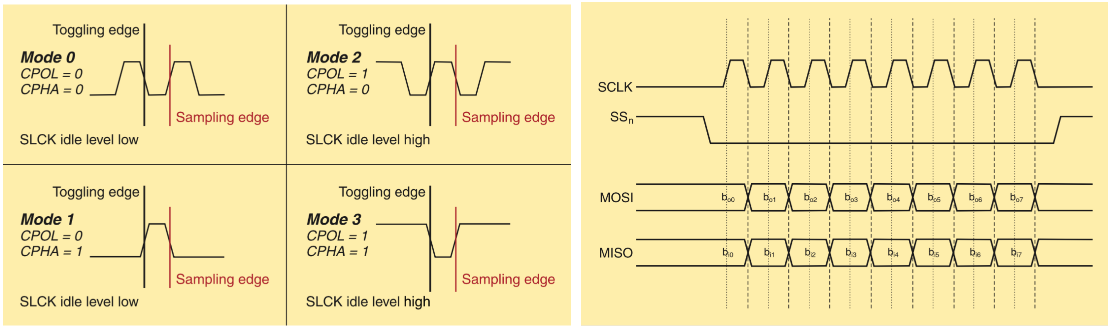

(a) (b)

Figure 3.9: SPI communication signals: (a) SPI modes; (b) 4 signals in mode 0.

3.3.2 MSP430G2553

As mentioned at the beginning of Section 3.3, the microcontroller used for setting the registers of the PLL is the MSP430G2553 [47]. The latter was initially bought with the MSP-EXP430G2ET Launchpad. This MCU is characterized by 24 GPIOs (general purpose input output) and two universal serial communication interfaces USCI_A and USCI_B, both supporting the SPI. The package of the MCU is characterized by 20 pins as in Fig 3.10.

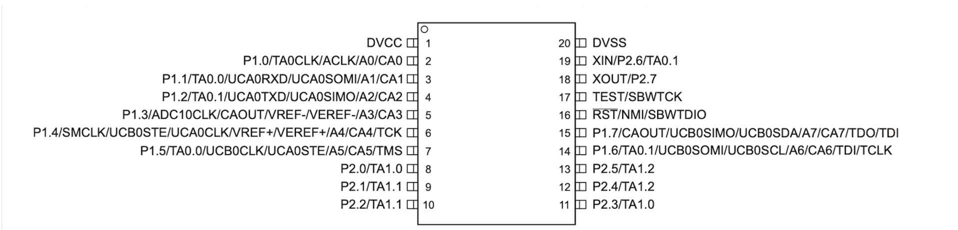

Figure 3.10: 20-pin Package of the MSP430G2553

TI's MSP-EXP430G2ET has a eZ-FET debug probe that allows cheaply to dubug the MCU. The eZ-FET provides a UART-USB interface through which it is possible to connect the PC for dubugging. The debug probe is connected to the MCU with isolation jumper blocks. The jumpers can be disconnected to program and debug another MCU as it will be shown in section 4.2.

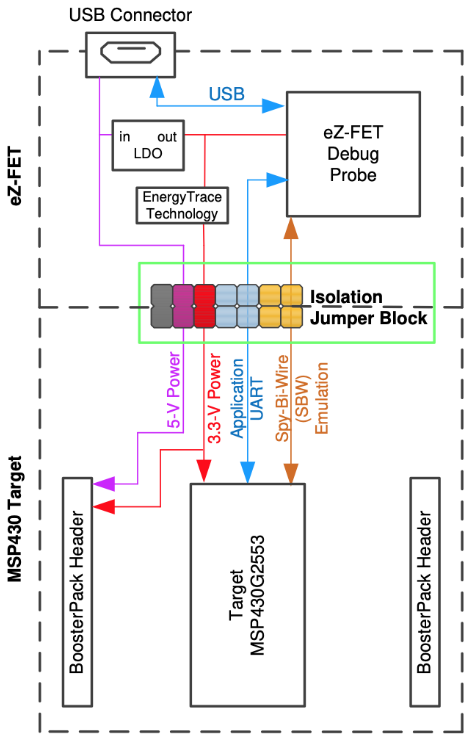

Figure 3.11: Connection between MSP430 and the eZ-FET debug probe.

The eZ-FET provides also, with its USB connection to the PC, the power of 3.3 V to the MCU as well of 5 V to the BoosterPack Header.

3.3.3 Program to set PLL registers

When programming the PLL with the SPI protocol, the MCU is the master, while the PLL is the slave. The serial bus of the LTC6948 is made by the four SPI signals: $\overline{\text{CS}}$ ($\overline{\text{SS}}$), SCLK, SDI (MOSI), and SDO (MISO). To enable the communication, the PLL must receive from the master a low $\overline{\text{SS}}$. The input data of the slave is clocked at the rising edge and every byte is sent with the most significant bit (MSB) first. In order to set the write or read mode of a register, the master must send a byte composed by seven bits identifying the register address and the last significant bit (LSB) with a "0" for the write mode and a "1" for the read one. One efficient way to send the data is to use the multiple byte transfer exploiting the auto-increment of the register addresses. This method is accomplished by sending the first register address in the first byte, with its data in second one, and continuing sending bytes that are destined to the subsequent registers.

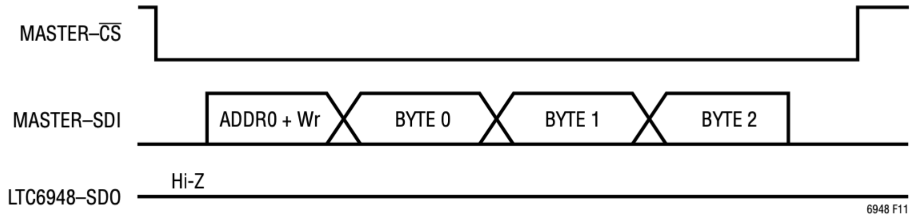

Figure 3.12: Auto-increment in write mode to fill the registers of the PLL.

The registers of the PLL has already been shown in Section 3.2.2. Using the auto-increment mode illustrated in Fig. 3.12 the bytes that have to be sent are fourteen and are the ones in Tab. 3.4.

	MSB	**[6]**	**[5]**	**[4]**	**[3]**	**[2]**	**[1]**	**LSB**
1st Addr + write	0	0	0	0	0	0	1	0
Data Byte 1	0	0	0	0	0	1	0	0
Data Byte 2	0	0	0	0	0	1	0	0
Data Byte 3	0	0	1	1	1	1	1	0
Data Byte 4	0	0	1	0	1	1	0	0
Data Byte 5	0	0	0	0	0	0	0	1
Data Byte 6	0	0	0	0	1	0	0	0
Data Byte 7	1	1	0	0	0	0	0	0
Data Byte 8	0	0	0	0	0	0	0	0
Data Byte 9	0	0	0	0	0	0	0	0
Data Byte 10	0	0	0	1	0	0	0	0
Data Byte 11	1	1	1	1	1	1	1	0
Data Byte 12	0	0	1	0	1	1	0	1
Data Byte 13	0	0	0	0	0	0	0	0

Table 3.4: Fourteen bytes sent to the PLL to write its registers.

The writing communication occurs as in Fig. 3.13.

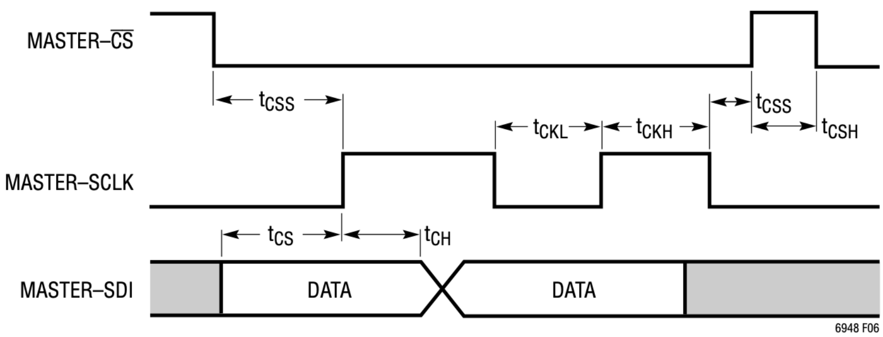

Figure 3.13: Write Timing Diagram of the PLL.

The SPI program was written (code is reported in Appendix A.2) using the USCI_B0 set as SPI mode with the SMLCK clock at 1 MHz which was then divided by 6 with a prescaler in order to obtain a clock period of 6 µs, equal to the one received from the demo board for programming. The SPI of the MCU is set in master mode since it is the one that will send the clock for the synchronous communication and the data. Within the other settings it is possible to find the MSB set as the first bit to be sent, the slave enabled when the $\overline{\text{SS}}$ is low and the clock phase and clock polarity set respectively to "1" an "0". All the SPI ports are set for the purpose (P1.4, P1.5, P1.6, P1.7). In order to start sending the packages, a timer (TimerA) was set in such a way that, when the counter reaches its overflow, the program is interrupted by a service routine that fills in parallel the transmitter buffer with the bytes and shifts out serially bit by bit. The timer is set with a SMCLK clock, divided by 8 (8 µs period). Since the timer counter is made of 16 bits which corresponds to a total value of 65535, the time it takes to reach overflow with 8 µs clock period is approximately 0.5 s.

The whole time it takes to send the signals is approximately 700 µs, considering the clock and the amount of bytes that are sent:

$$Time = Period \cdot Bytes \cdot Bits = 6\,\mu s \cdot 14 \cdot 8 = 673\,\mu s \tag{3.5}$$

During the period of signal sending, the green LED on P1.0 was configured in order to switch on, to verify that the signal has been sent.

3.4 PCB design: from schematic to layout

The design of the PCB has been done with Altium Designer, starting from the schematic, selecting between all the available components and then developing the layout. When designing a PCB it can be easier to know a priori who will manufacture and assemble the PCB, in order to satisfy the production rules and to choose between the available components. In the case of this work, the company chosen for manufacturing and assembly was Eurocircuits.

3.4.1 Overview of the schematic

The overall schematic (Fig. 3.14) of the transmitter was done in order to be able to test every single block separately and to eventually bypass a non-working component. This was done with the insertion of UFL connectors and the use of headers. Almost all the blocks are powered with 3.3 V and 5 V, while the ASK needs also −5 V and the PA 2.8 V, but the latter will be provided with a voltage regulator. The schematic of the Pierce oscillator and the T-Pad were drawn accordingly to the LTSpice simulations, while the other blocks were designed following the datasheet with a lot of care to the high-frequency components. More attention was paid to the schematic of the microcontroller that was completely re-adapted for this design. To set the registers of the PLL two methods have been implemented: the use of the microcontroller and the use of the interface already present on the LTC6948 Evaluation Kit to allow the connection to the programming demo board.

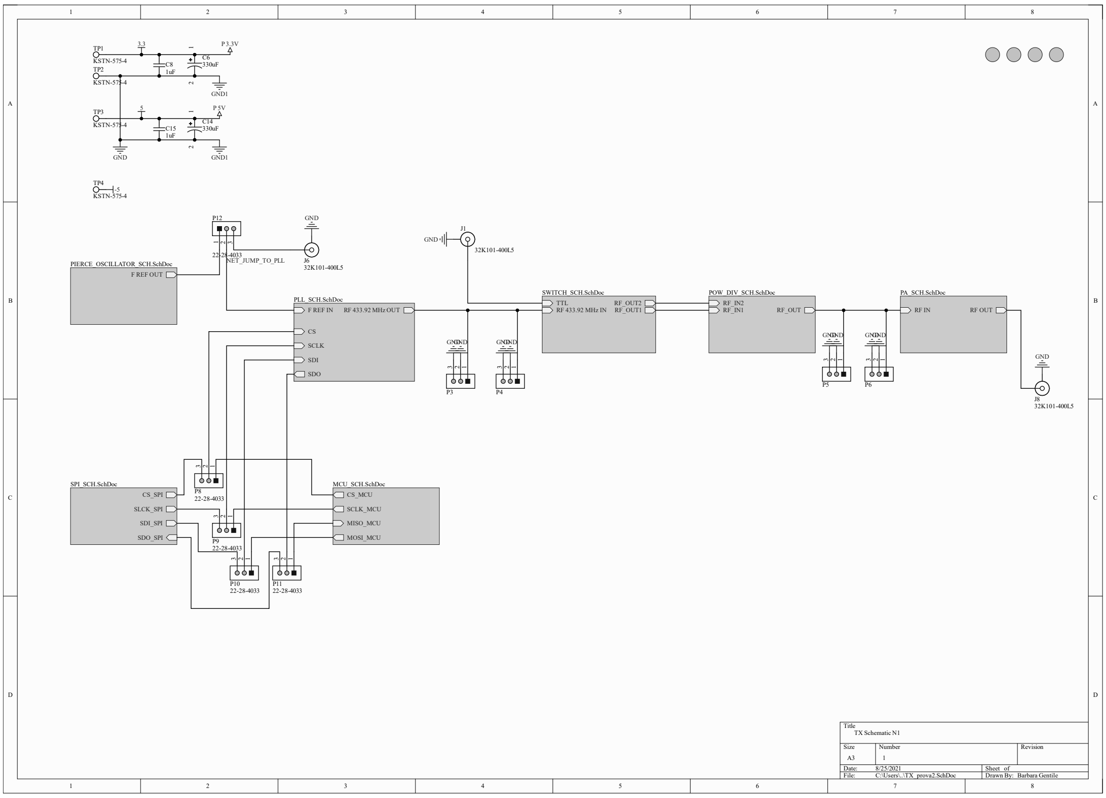

Figure 3.14: Altium Schematic of RF SWIPT Base Station.

Microcontroller integration

The microcontroller was inserted in the PCB as in Fig. 3.15. In order to integrate the microcontroller in the PCB while keeping the possibility to program it from the outside, one method is to insert the same header (P1) as the isolation block shown in Fig. 3.11. In this way it is possible to connect the eZ-FET Debug Probe directly to the microcontroller of interest and program it. Once programmed, the MCU will keep the information on its memory until re-programmed. Moreover the pads that are used for the USCI_B0 were connected to the headers (P8, P9, P10, P11 in Fig. 3.14) to allow the connection to the PLL. Between the MISO/SDO and GND a resistor of 200 kΩ was added as recommended in the PLL datasheet to ensure that the line returns to a state which is known in the Hi-Z state. Tab. 3.5 reports the pins reserved for the interface USCI_B0 that are used for the SPI.

Pin	Port
6	UCB0STE
7	UCB0CLK
14	UCB0SOMI
15	UCB0SIMO

Table 3.5: Pins for SPI communication with USCI_B0 of the MSP430G2553.

A reset button was also added to pin 16 to allow to re-send the SPI signals at any time, while two green LEDs were placed at pins 2 (PORT 1.0) and 8 (PORT 2.0) to allow the user see when the signals are sent, as it was done with the MSP Launchpad (Section 3.3.3). The remaining pins were brought outside the PCB with the header P2, in order to be able to use them if needed.

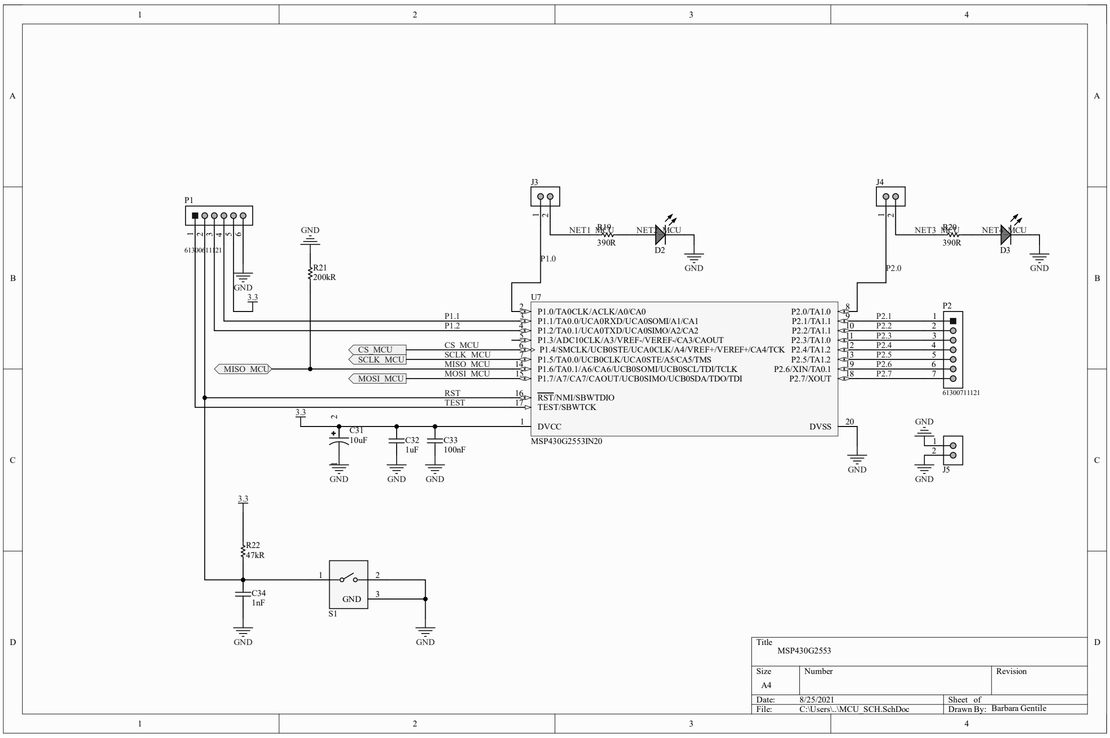

Figure 3.15: Altium Schematic of the Microcontroller.

Voltage regulator for PA powering

The power of the PCB is given with banana connectors for the 3.3 V, 5 V and −5 V, while the 2.8 V is provided to the PA with a voltage regulator, being only a bias voltage that drives 4.5 mA of current. Between the switching and linear voltage regulators the preferred one for low load currents is the linear one, being simple and adapt for output voltages lower than the input ones [48]. The regulator chosen for the PA is the low-dropout (LDO) TPS7A2028PDBVR by Texas Instrument that can source up to 300 mA of current and receive an input voltage from 1.6 V to 6 V.
The input voltage of the regulator was chosen to be 3.3 V, since the lower it is, the lower is the power dissipation (Eq. 3.6).

$$P_{diss} = (V_{in} - V_{out}) \cdot I_{load} \tag{3.6}$$

The regulator receives also an enable signal that is needed to activate the drop-out. The drop-out is enabled with voltages higher than 1.6 V and the inputs can reach a maximum of 6.5 V. For this purpose, also the enable voltage was set to 3.3 V.

3.4.2 Layout choices

The importance of the 50 Ω matching becomes relevant when working on the PCB layout. Considering a $\epsilon_{eff} \approx 4$, which is typical for the FR4 substrates, the critical length obtained from Eq. 2.2 is close to 2 cm. Since the RF traces are comparable or longer than 2 cm, it is necessary to build the traces guaranteeing the 50 Ω impedance in order to deliver the maximum amount of power to any of the loads. For this PCB, the geometry chosen for the traces is the microstrip one. As highlighted in Fig. 2.4, the characteristic impedance depends mostly on the thickness of the substrate and the width of the trace. A thinner substrate allows to have narrower traces. Fortunately, Altium Designer is provided with a calculator that follows the IPC-2252 standards to calculate the characteristic impedance of the trace. After defining the PCB layer stack with all the layers thickness and the dielectric constant, it is possible to create a net class "RF" and set its impedance to the desired value. The PCB has been designed to be fabricated from Eurocircuits which allows to choose between many different thicknesses. The chosen substrate was the Isola 400 FR4, 0.36 mm thick. This improved FR4 was chosen for its high reliability and because its electrical were well defined: dielectric constant D_k=3.90 and dissipation factor D_f=0.022.

The layer stack is shown in Fig. 3.16, the PCB is made of only two layers for simplicity.

#	Name	Material	Type	Weight	Thickness	Dk
	Top Overlay		Overlay			
	Top Solder	Solder Resist	Solder Mask		0.01016mm	3.5
1	Top Layer		Signal	1oz	0.03556mm	
	Dielectric 1	FR-4	Dielectric		0.35999mm	3.9
2	Bottom Layer		Signal	1oz	0.03556mm	
	Bottom Solder	Solder Resist	Solder Mask		0.01016mm	3.5
	Bottom Overlay		Overlay			

Figure 3.16: Layer Stack Manager of the PCB.

Once the thickness of the board has been defined, the next step is to derive the correct width of the traces to have the $50\,\Omega$ characteristic impedance. The parameters of the microstrip that were chosen with the Altium calculator tool are shown in Fig. 3.17.
With a trace width of $0.71\,\text{mm}$, an impedance of $49.98\,\Omega$ is reached.

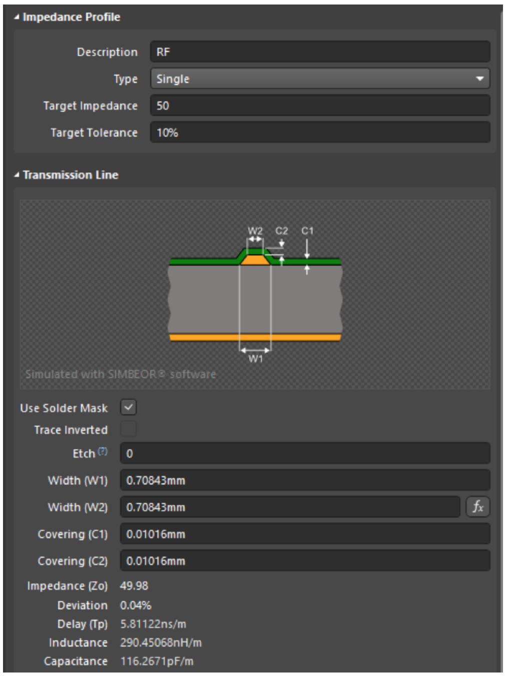

Figure 3.17: Microstrip parameters for RF traces in the PCB to obtain $50\,\Omega$ characteristic impedance.

As explained in Section 2.1.3, the signal travels thanks to the coupling between the trace and the reference plane. The layout was designed in order to have always the ground plane below the high frequency conducting traces and to avoid any cross between the lines. The ground plane was then distributed in both the lower and upper layer, excluding the connecting wires, and connected together with vias. The via stitching is a technique that consists in distributing many vias all over the PCB to create a strong vertical connection to maintain low impedance and short return loops [49]. Besides the via stitching, what it is also convenient to place in a high frequency design is the via shielding around the RF traces, in order to reduce the crosstalk and electromagnetic interference.

Design Rules Check

One of the most important facts that must be considered when designing a PCB is to respect the rules of the manufacturing company. A violation of the rules can lead to wrong connections and to a complete malfunctioning of the board. Between the rules it is possible to find, for the outer layers, the minimum acceptable distance from track to track, track to pad, pad to pad and the minimum track width and annular ring for the vias. Other rules concern the solder mask openings distances. Solder mask is fundamental when assembling a PCB because it rejects the solder, avoiding to short circuit the pads or traces. Other minor rules regard the silkscreen text, that should not be too small and too close to the solder mask openings. After having considered all the rules, the final design from the top looked as in Fig. 3.18.

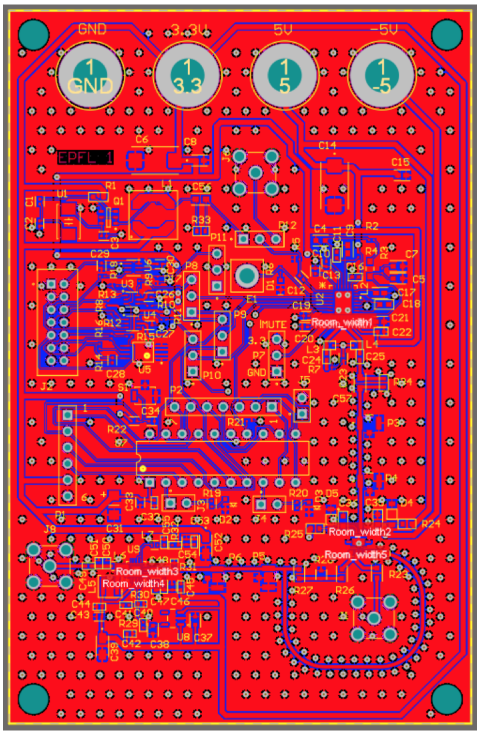

Figure 3.18: PCB layout of RF SWIPT base station (top view).

Chapter 4

PCB Experimental Results

4.1 Manufactured PCB

The printed circuit board for the RF SWIPT base station was manufactured and assembled by Eurocircuits and the final product is the one in Fig. 4.1.

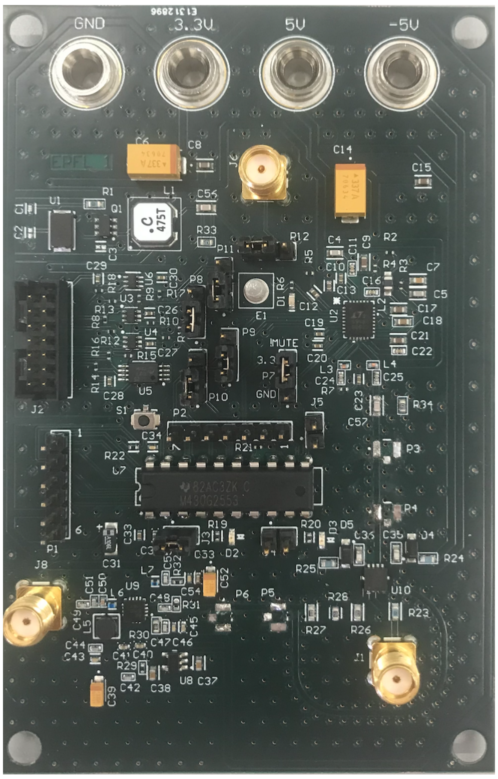

Figure 4.1: Manufactured and assembled PCB for RF SWIPT base station.

From the image of the manufactured PCB it is possible to observe all the connections that were made through the headers and connectors. The UFL testing points were later removed. The PLL receives the input signal from the quartz crystal which is connected with P12, with the possibility to switch the pin and obtain an external signal at any frequency from the SMA connector J6. The microcontroller is linked to the PLL with P8, P9, P10, P11 and, switching the positions of all the bridges it is possible to connect the SPI interface for the external programming board. The 6 pins header P1 allows the programming of the microcontroller as will be shown in Section 4.2. Header P7 allows to turn on the output of the PLL and it was necessary when the component was programmed with the demo board, but was found useless when sending directly the signals from the MCU. J2 is the same header taken from the Evaluation Kit of the PLL to connect the programming board but it was not used since the the registers were filled successfully by the MCU. The remaining connectors are J1 and J8. J1 allows to control the position of the switch for the ASK modulation and the signal is given from a waveform generator at a desired frequency. J8 is used to extract the output of the power amplifier and either measure it at the oscilloscope or connect it to a printed coil.

4.2 Microcontroller Programmed with MSP-EXP430G2ET Launchpad

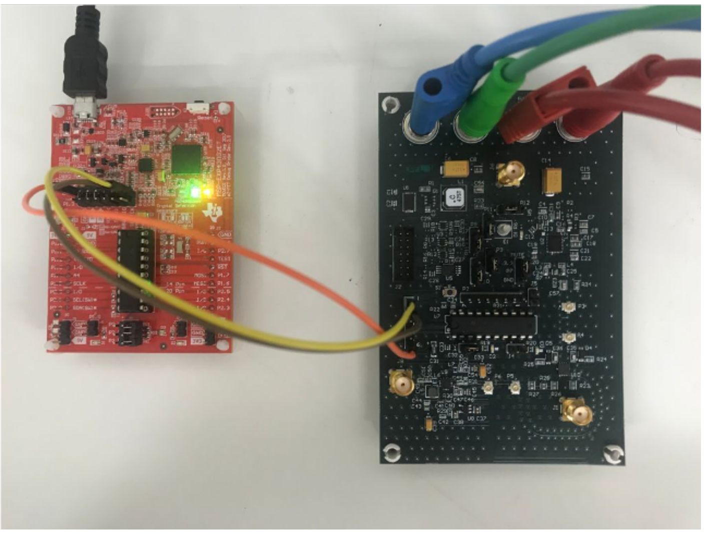

Figure 4.2: MSP430G2553 programmed with eZ-FET Onboard Debug Probe connecting *GND*, *STBWDIO* and *SBWTCK*.

The microcontroller assembled on the PCB needs to be programmed the first time the PCB is used and will keep the program for the entire life of the product. To program the MCU, the eZ-FET Onboard Debug Probe of the Launchpad was connected to the following pins of the MSP430: *GND*, *STBWDIO*, *SBWTCK* (Fig. 4.2). With this method, when launching the program from the PC with Code Composer, the latter is saved on the connected MCU rather than the microcontroller on the Launchpad. To correctly launch the debug, the PCB must be powered up. To verify that the debugging of the on-board MCU was working, a first try was done with the code of a blinking led, since two LEDs were placed in PCB. Once verified, the proper program for the PLL register setting was saved on the MCU. Once the microcontroller is programmed, every time the board is switched on, it sends the three signals to the PLL to fill its registers and lock it. Otherwise it is always possible to re-send the signals using the reset push-button. To verify the signals sent from the MCU, three probes were connected from the headers P8, P9, P10 to the oscilloscope to verify, once powering the MCU, what was the SPI output (Fig. 4.3).

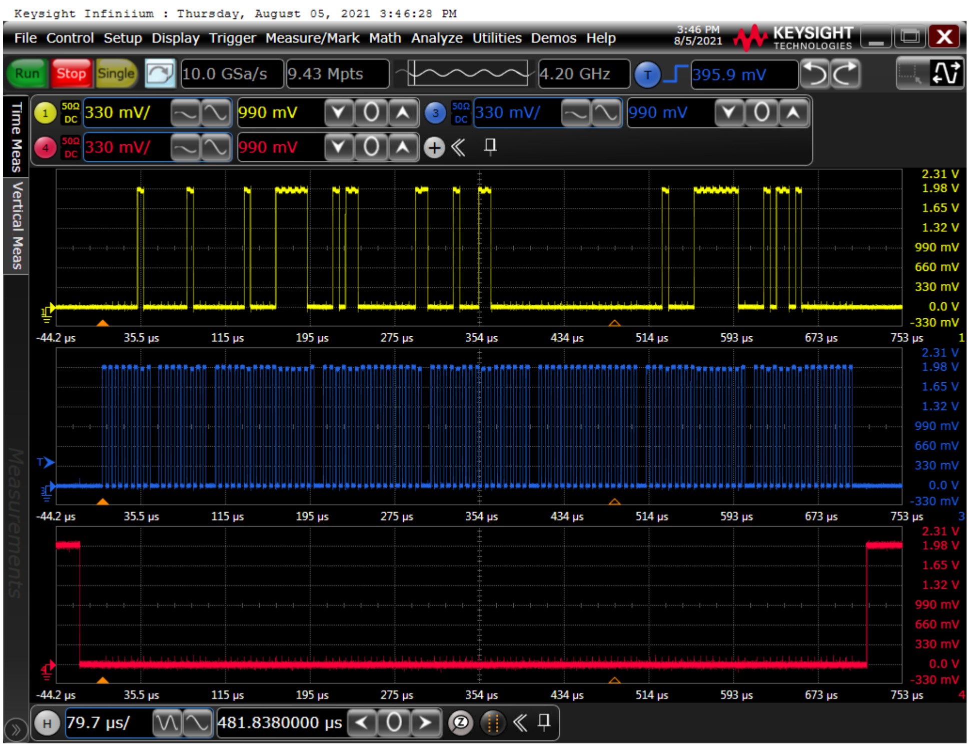

Figure 4.3: SPI signals observed with single acquisition at the oscilloscope.

4.3 Signal measuring

All the signals were taken either connecting the oscilloscope in parallel to the circuit with 1 MΩ or at the end of a block with 50 Ω. To better analyze the separated blocks, and the matching of the traces, some traces of the PCB were cut. The oscillation of the quartz is observed at the digital storage oscilloscope (DSO), ending the line at 50 Ω. The results are shown in Fig. 4.4. Removing the capacitors from the Pierce was successful for the oscillation of the quartz.

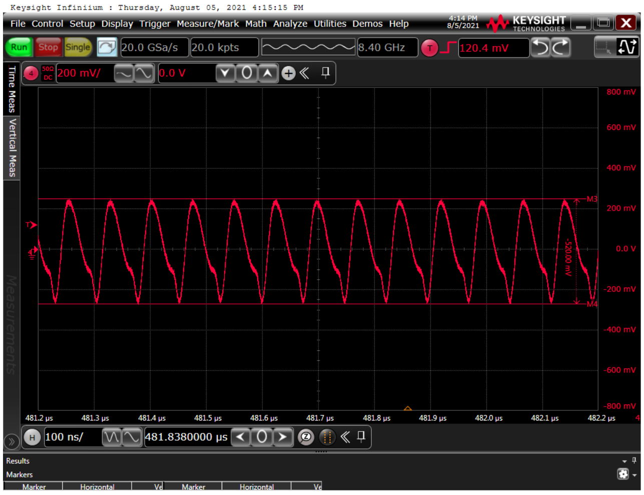

(a)

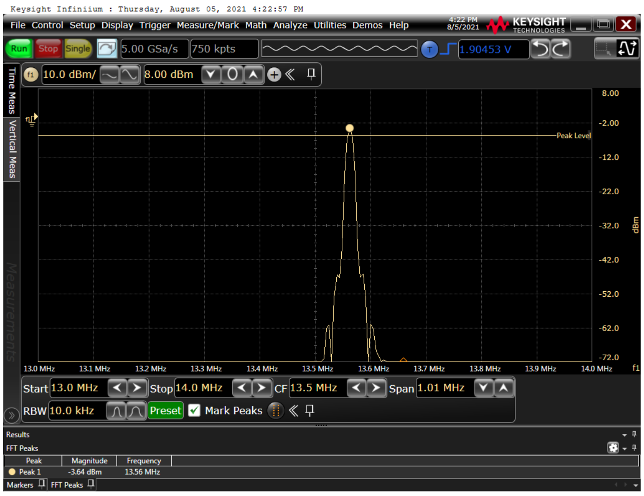

(b)

Figure 4.4: Pierce oscillator output. a) Waveform with V_{pp}=520 mV; b) FFT with peak at 13.56 MHz.

If the reference frequency (13.56 MHz) is given as input to the PLL, either from the quartz or from an external source, and its registers are filled in the correct way, the PLL passes to the *lock* state. With the registers set as in Tab. 3.4, the *lock* state can be seen at pin 2. Using as reference signal the output of the quartz, the signal is locked at 433.96 MHz which is included in the ISM band [433.05÷434.7] MHz. The maximum output power from the single-ended PLL, 1.5 dBm, was set filling RFO[1:0]=11 and it corresponds to 750 mV$_{pp}$ if the load is 50 Ω. The output of the PLL is observable in Fig. 4.5.

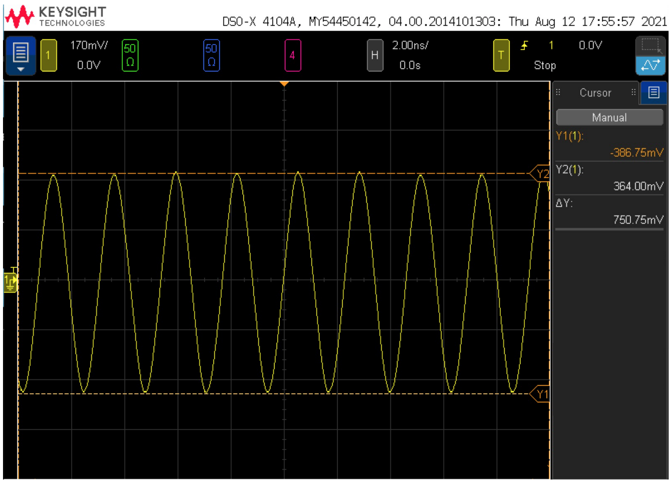

(a)

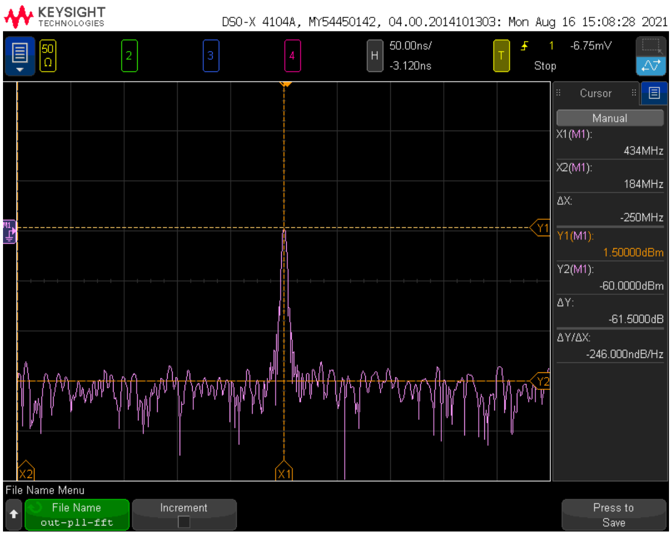

(b)

Figure 4.5: PLL output. (a) Waveform with V$_{pp}$=750 mV; (b) FFT with peak at 1.5 dBm at 433.96 MHz.

The output of the PLL, together with its *lock* state, confirms that also the MCU is correctly sending the data. Moreover, the PLL is built with two RF outputs, in order to use it either in differential or in single-ended mode. In the project it has been used in single-ended mode using RF^{+}, and closing RF^{-} with a resistance of $50\,\Omega$. Measuring simultaneously the two exits, it is possible to observe two equal outputs with a opposite phase (Fig. 4.6).

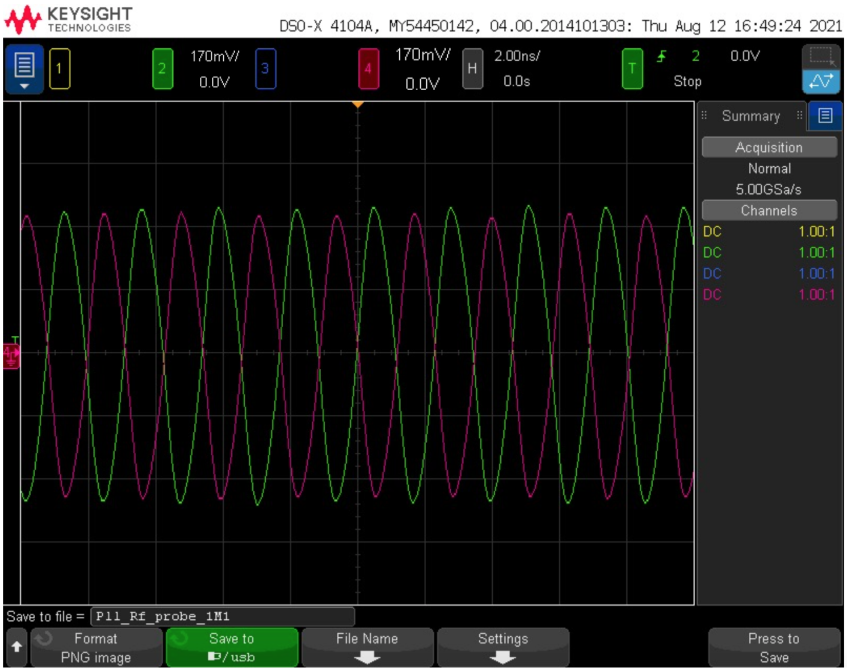

Figure 4.6: Differential output of PLL.

The ASK generates a reflection of the signal due to the fact that, after the switch, there is an intersection between the lines, hence the traces see a discontinuity. This problem can be solved placing two switches in such a way the traces never intersect. The improvement is shown in Section 7.1.
To still test the attenuation of the T-Pad in the correct way, the PCB trace was interrupted after the T-Pad and before the intersection. After the T-Pad, the power of the signal is the expected one: 499 mV and the attenuation is correctly 3.5 dBm. The attenuated signal after the T-Pad is shown in Fig. 4.7.

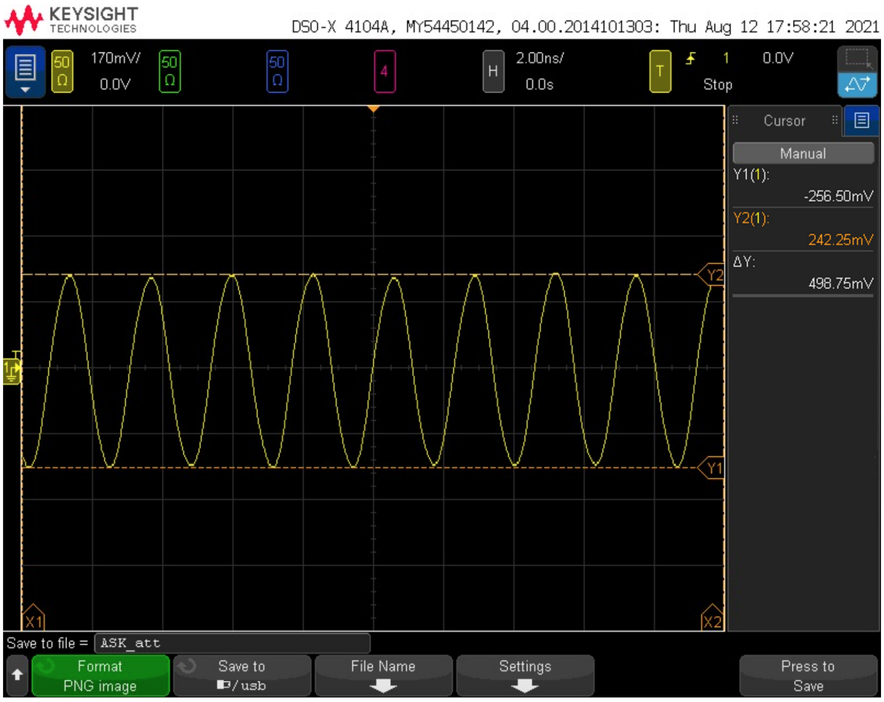

Figure 4.7: T-Pad output: waveform with V_{pp}=499 mV.

The power amplifier was optimized to work at 450 MHz. The optimization can be seen providing the input from a signal generator and sweeping the frequencies. The input power that was used for the measurement is -6dBm. Moreover, the DC input power of the PA was measured to verify the correct functioning of the voltage regulator and the measured value was 2.8 V, as expected.
The images in Fig. 4.8 were taken with the same x and y scales in order to see the differences in terms of frequency and wave amplitude. The difference between the circuitry of the Evaluation Kit and the one designed on the PCB is very evident. The Evaluation Kit was tuned to work at 900 MHz, while in the case of the PCB design, the amplification at frequencies higher than 700 MHz is null. From the sweep it is possible to see that the highest amplification is reached between 300 MHz and 500 MHz.

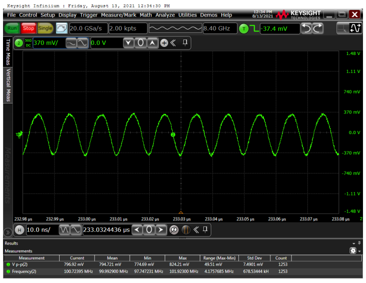

(a)

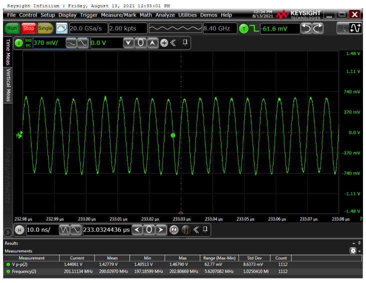

(b)

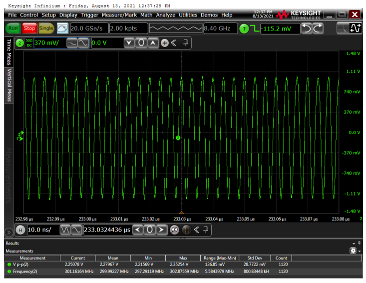

(c)

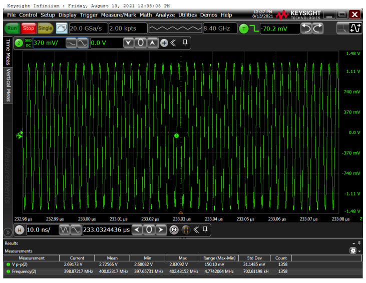

(d)

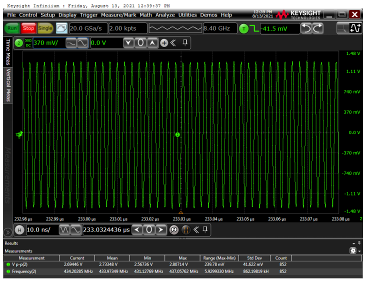

(e)

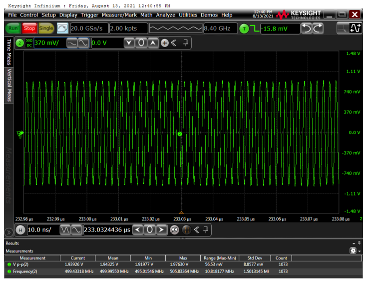

(f)

(g)

(h)

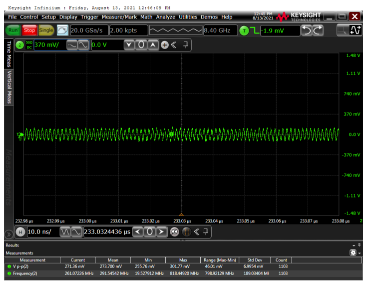

(i)

Figure 4.8: Power Amplifier output sweeping the input frequency with -6 dBm input. (a) 100 MHz, (b) 200 MHz, (c) 300 MHz, (d) 400 MHz, (e) 433.92 MHz, (f) 500 MHz, (g) 600 MHz, (h) 700 MHz, (i) 800 MHz.

To test the gain of the Power Amplifier, different input voltages were applied with the generator, while maintaining the frequency fixed at 433.92 MHz. The gain obtained by varying the input power is reported in Tab. 4.1. All the measures are taken placing a 10dBm attenuator to avoid the damaging of the DSO.

In Power	**Out V_{pp} on 50 Ω**	**Out Power**	**Gain**
-10 dBm	6.32 V	20 dBm	30 dB
-8 dBm	7.96 V	22 dBm	30 dB
-6 dBm	9.5 V	23.5 dBm	29.5 dB
-4 dBm	10.024 V	24 dBm	28 dB
-2 dBm	12 V	25.5 dBm	27.5 dB
0 dBm	14.16 V	27 dBm	27 dB
2 dBm	16.83 V	28.5 dBm	26.5 dB
4 dBm	17.82 V	29 dBm	25 dB
6 dBm	17.9 V	29 dBm	24 dB

Table 4.1: Gain of the Power Amplifier as funtion of the input power.

The output power is derived from the V_{pp} using Eq. 4.1 and 4.2.

$$P_{(mW)} = \frac{V_{rms}^2 \cdot 10^3}{R} \tag{4.1}$$

$$V_{rms} = \frac{2 \cdot V_{pp}}{\sqrt{2}} \tag{4.2}$$

To derive the power in dBm, the equation is the following:

$$P_{(dBm)} = 10\log(P_{(mW)}) \tag{4.3}$$

The overall output of the PCB with the modulated wave is shown in Fig. 4.9. The digital signal is given from a waveform generator to the switch through the SMA connector J1. From the image it is possible to observe that when the external signal is 0, the amplitude is reduced. The sequence of bit is an arbitrary one that was created on Excel and saved on the generator.

Figure 4.9: PCB output with arbitrary digital signal as input.

The total output power that the PCB can reach, without passing through the T-pad attenuator, is 28.5 dBm, which corresponds to 700 mW.
The absorbed power by the whole PCB is reported in Tab. 4.2, considering the input voltages provided by the generators.

Voltage	Current	Power
3.3 V	722 mA	2.6 W
5 V	40 mA	200 mW
-5 V	2 mA	10 mW

Table 4.2: Absorbed power for the different values of voltage.

The total absorbed power is 2.59 W.
An ultimate test was done sweeping the frequencies of the digital signals from 1 Mbps to 10 Mbps. In any case the digital "0" and "1" can be distinguished but when the frequency is higher, the rising and falling time of the digital waveform generator becomes more evident. A visual example of the influence of the rising and falling time on the modulation at low and high rate in given in Fig. 4.10.

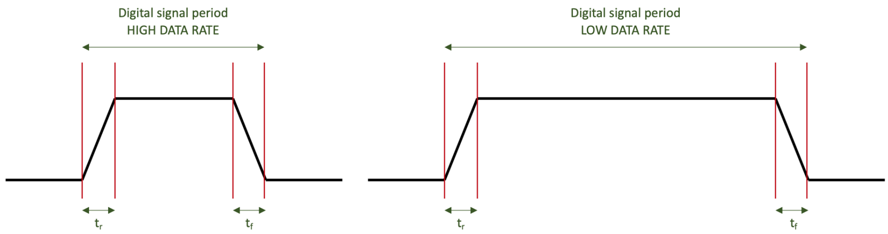

Figure 4.10: Influence of rising and falling time of the waveform generator on the signals with high and low data rate.

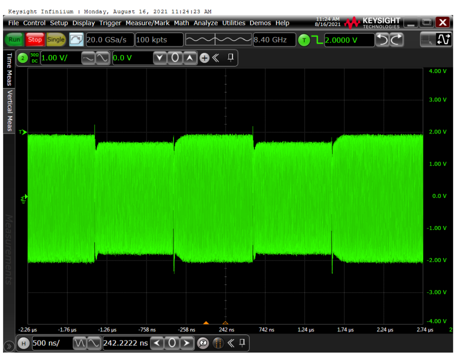

(a)

(b)

(c)

(d)

Figure 4.11: PCB output with arbitrary digital input at increasing frequencies. (a) 1 Mbps, (b) 2 Mbps, (c) 4 Mbps, (d) 10 Mbps; x and y scales of the oscilloscope are equal for all the measurements.

Chapter 5

Inductive power transfer: 3 coils inductive link

The 3-coil IPT link allows to reach high values of PDL and PTE and to homogeneously distribute the power over a greater area and for these reasons, it was preferred with respect to the others for this application. In this Chapter, the work done to optimize the inductive link efficiency and the study about the microfabrication processes will be presented. The attention was given mostly to the resonator coil, that is characterized by many constraints, since it has to be implanted in the brain, close the the receivers. In particular, an optimization of the shape was done in order to fabricate the desired resonator coil.
The overall work was done as follows:

1. Simulations to find the optimal shape and encapsulation material to maximise the quality factor of the coil implanted into the brain at 433.92 MHz;

2. Microfabrication of the optimal shape with little modifications to give the possibility to attach a SMA connector to test the S-parameters with a Network Analyzer;

3. Simulation in air of the exact shape of the microfabricated coil;

4. Check if simulations coincide with the fabricated coil to verify that the simulations are reliable and the in-brain resonator will work as expected.

In addition, some printed coils were fabricated to easily test the transmission of the PCB.

5.1 Simulation study for optimization of resonator quality factor

The simulations of the coil's parameters were done with Ansys HFSS. A first study was done to optimize the quality factor of the resonator coil which is a key-factor for the improvement of both PDL and PTE (Fig. 2.8). The optimization of Q was done considering the shape of the coil, with its overall size and width.
The simulation design was done considering the following multi-layer brain model with the respective thicknesses:

Skin	2 mm
Fat	2 mm
Muscle	4 mm
Skull	10 mm
Dura Mater	1 mm
Cerebro Spinal Fluid	2 mm
Brain Gray Matter	20 mm

Table 5.1: Multi-layer model of brain.

The Ansys HFSS model looks as in Fig. 5.1.

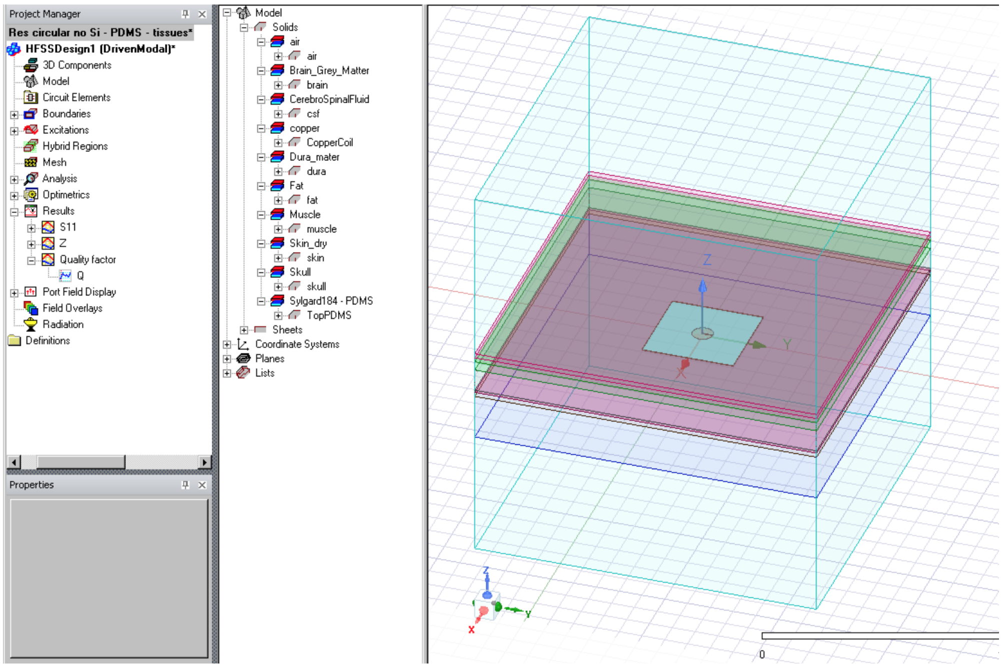

Figure 5.1: Ansys HFSS model with brain layers.

Many shapes were simulated and optimized with the same external condition: equal brain layers, equal copper thickness (25 µm), equal encapsulation material and thickness: polydimethylsiloxane (PDMS) 200 µm. In particular, the analyzed shapes were: square, hexagonal, square with inside cross and circular. To perform the simulation, a rectangular lumped port was placed in correspondence of the coil aperture. All the analyzed coils are made by a single turn to keep the SRF high enough to work at 433.92 MHz. For any configuration, two main sweeps were applied: the diameter/edge size of the coil and its width. After defining the best sizes for the highest quality factor, the quality factors of the different shapes were compared and the highest one was found to be the circular one. Even if the quality factor was found to be higher for smaller coils, the lower limit in terms of diameter/edge was fixed at 9 mm in order to be able to cover a large area of implanted electrodes. The highest quality factors that were found for the different shapes at 433.92 MHz are reported in Tab. 5.2 while the simulation models are reported in Fig. 5.2.

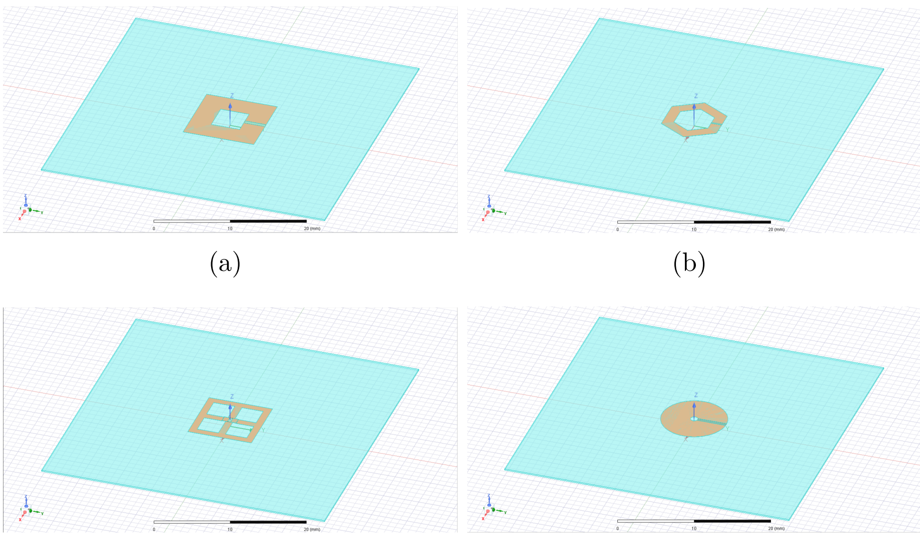

(a) (b) (c) (d)

Figure 5.2: Simulation with different shapes. The brain layers are hidden to allows a better view of the coils. (a) Square, (b) hexagonal, (c) square with inside cross, (d) circular.

The highest quality factor is given with a circular coil of external diameter 9 mm and width 4 mm placed between the cerebro spinal fluid. Also the square shape with the inside cross is very promising, the quality factor is lower but its square shape allows to cover a bigger area. However, the rest of the analysis was done considering the circular one.

Shape	Quality factor @ 433.92 MHz
Square	13.36
Hexagonal	24.50
Square with inside cross	45.45
Circular	63.13

Table 5.2: Best quality factors obtained at 433.92 MHz optimizing different coil resonator shapes.

A second simulation was done for the encapsulation material. The encapsulation must be made of a biocompatible material because it is in direct contact with the tissues and the whole system must be thin and flexible. Considering the biocompatibility and the ease of microfabrication, two materials were considered: PDMS and polyamide. Fig. 5.3 suggests that higher values of quality factor are obtained with PDMS with large thickness. However, increasing the thickness of the material leads to lower flexibility and might become bothering for the implantation.

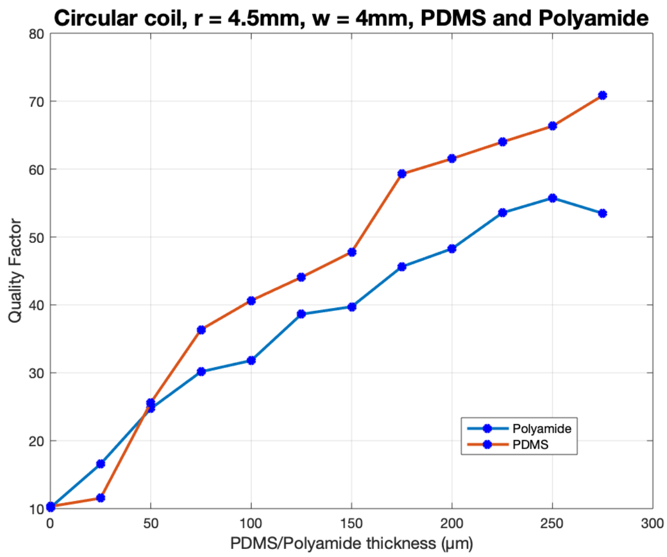

Figure 5.3: Quality factor vs. encapsulation thickess for PDMS and polyamide.

The trend of the quality factor is illustrated in Fig. 5.4 for the circular coil encapsulated in 200 μm of PDMS. As mentioned in Section. 2.2.2, the presence of the tissues highly reduces the Q, indeed the same PDMS encapsulated circular coil was simulated without the human tissues and the obtained quality factor was 117.95.

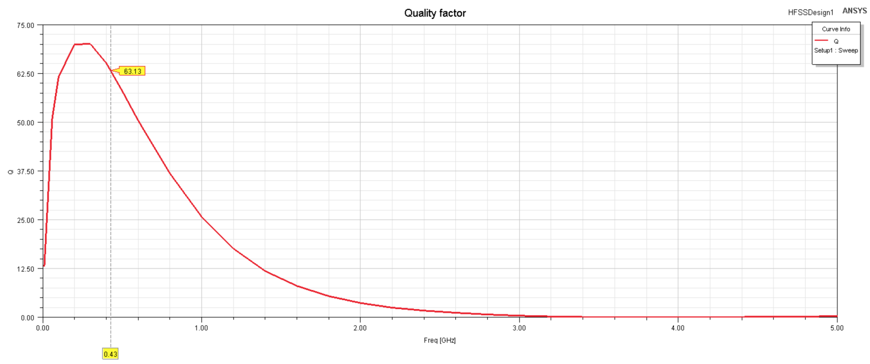

Figure 5.4: Quality factor of circular resonator between tissues vs. frequency.

An additional study was done adding the coil transmitter to the whole system containing already the optimized circular resonator and the tissues. The coil transmitter was designed to be printed on 1.55 mm of Isola 400 FR4 (D_k=3.9) and with the possibility to solder a SMA connector in order to connect the coil to the RF SWIPT base station. The selected copper thickness was 35 µm. Both the square and the circular shapes were simulated and, as for the resonator, it was found that the circular coil reaches higher values of Q. To maximise the quality factor, a sweep of diameter and width was performed. The optimal size for the quality factor was found to be: 14 mm diameter and 5 mm width. The model is shown in Fig. 5.5. The quality factors of the transmitter and the resonator are reported in Fig. 5.6, the resonator Q has lowered from 63.13 to 49.90 due to the presence of additional materials.

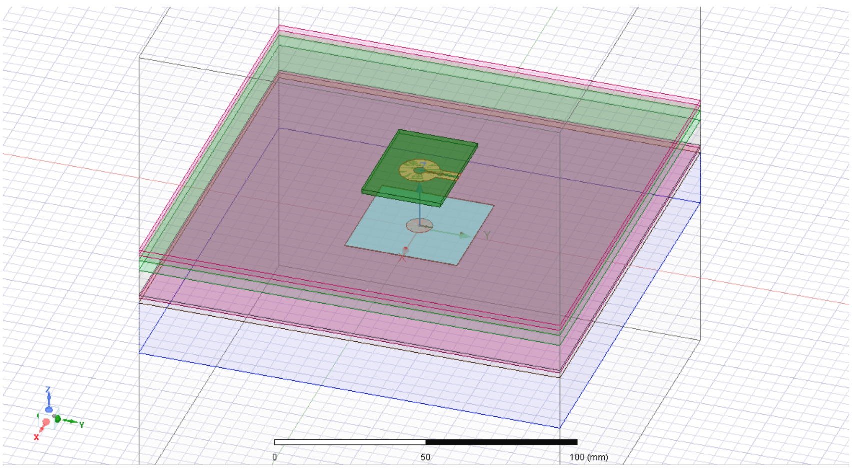

Figure 5.5: Ansys model with transmitter and resonator.

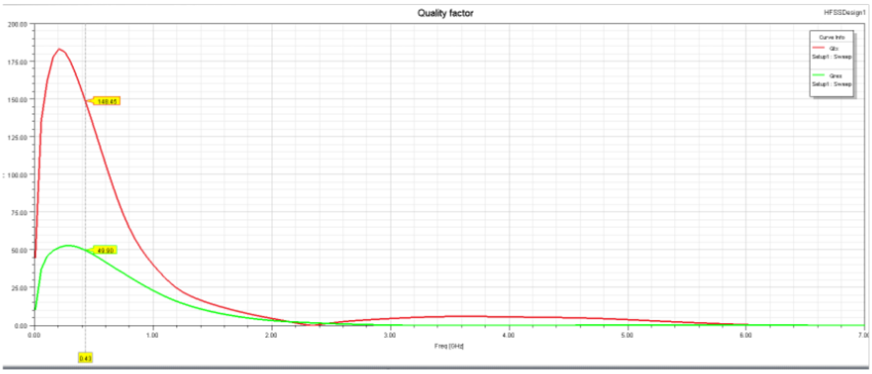

Figure 5.6: Quality factor of resonator and transmitter vs. frequency.

5.1.1 Research of capacitive value for minimization of return loss

When designing any inductive link, the LC tanks must resonate at the same operating frequency and the return loss should be minimized. With Ansys HFSS it is possible to add any lumped element in series or parallel by drawing a rectangle in the desired place. For this simulation, a parallel capacitor was added in correspondence of the resonator coil aperture and, sweeping the value of capacitance, it was possible to observe how the minimum peak of return loss moves toward lower frequencies by increasing the value of C_{res}.

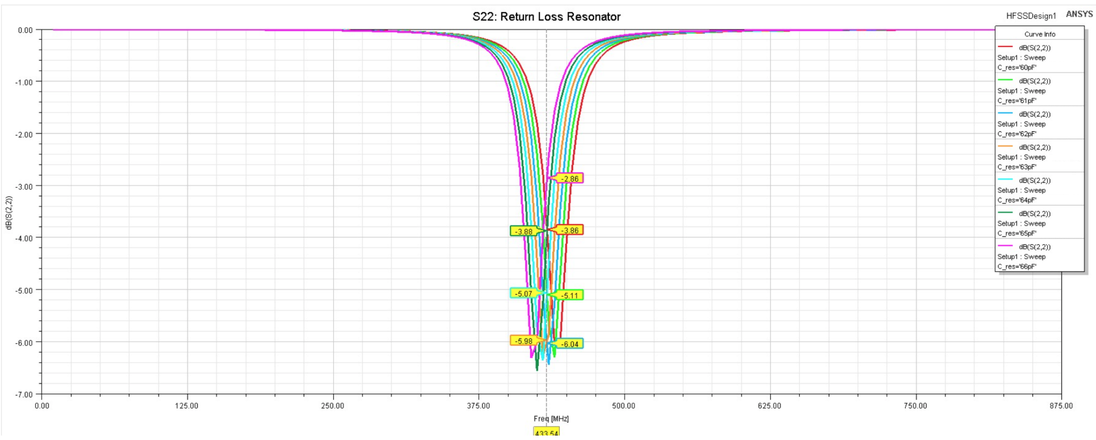

Figure 5.7: Return Loss shifted with parallel capacitor.

5.2 Fabrication of Resonator

The circular resonator coil was fabricated with same diameter and width of the simulated shape: 9 mm diameter and 4 mm width. However it was not totally encapsulated and two exposed strips of copper were added to facilitate the attachment of the SMA connector, to allow the measurements. To obtain the coil, a copper foil 25 µm thick, was cut at the laser cutter. The fabrication was done also for other shapes in order to study the feasibility of the process: a square coil with 10 mm edge and 3 mm width and another circular coil with 10 mm diameter and 3 mm width. The design of the coil for the laser cutter was done with AutoCAD and it is represented in Fig. 5.8. The purple layer is the one that has been cut, while the green represents the shape of the SMA connector that was added to the design to assure the possibility to attach the SMA once fabricated. Once the fabrication of the copper coils was over, some of them were sputtered with 10 nm of amorphous silicon on both sides to improve the adhesion of the coil to the PDMS layer, due to the Si-Si bonds.

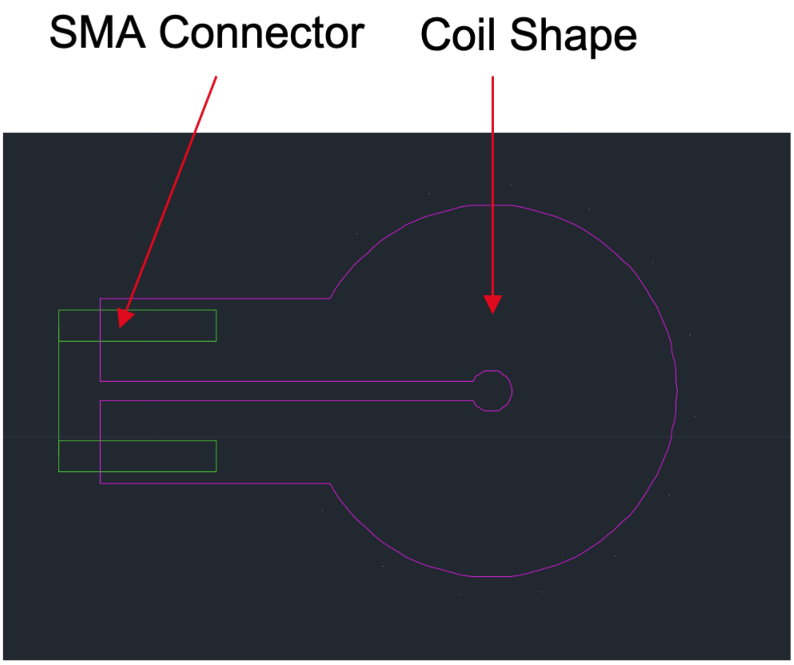

Figure 5.8: Autocad resonator design.

Due to the small internal radius of the coil, the encapsulating PDMS layer was built with an epoxy-based negative photoresist (SU-8) mold, to assure the attachment of the upper and lower layers of PDMS also in the middle of the coil. The SU-8 was chosen because it allows to have thicker structures with high aspect ratio and high resolution. Moreover, it is highly resistant to wet chemistry and cannot be stripped. In particular, the one that was used is the GM1070 by Gersteltec.
After spinning and baking the SU-8 on a clean silicon wafer, it was exposed in the same area included by the purple line in Fig. 5.8 in order to have, after the development in propylene glycol monomethyl ether acetate (PGMEA), a 25 µm elevation with the same shape of the coil.
In Fig. 5.9 it is possible to observe the SU-8 mold and its thickness, measured with the profilometer.

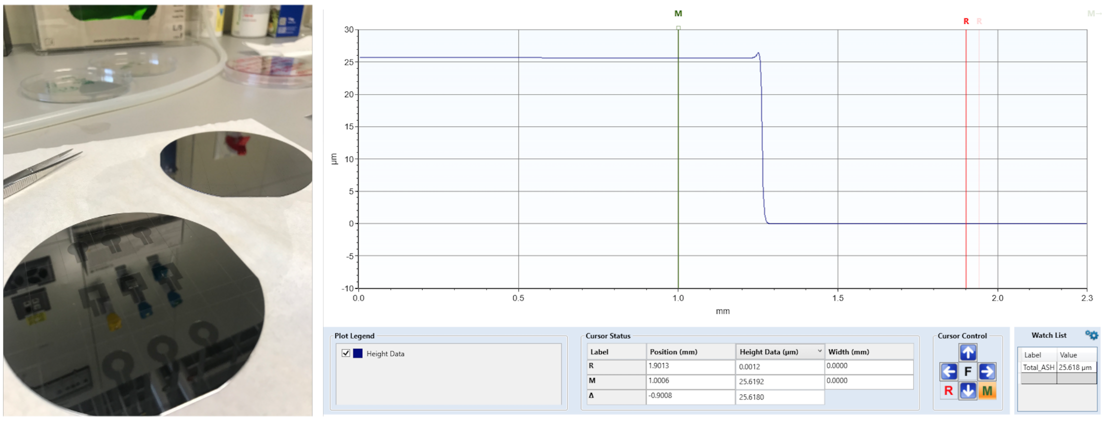

(a) (b)

Figure 5.9: SU-8 Mold. (a) Silicon wafer with SU-8 mold. (b) Profilometer measurement of the 25 µm mold thickness.

A polystyrene sulfonate (PSS) release layer was spinned over the SU-8 before spinning the 100 µm layer of PDMS. The same thickness of PDMS was spinned over a smooth silicon wafer with only PSS over it. The PDMS was cured in the oven for two hours at 75 °C, cut at the laser cutter in rectangular shapes for the encapsulation and then released in deionized water (Fig. 5.10).

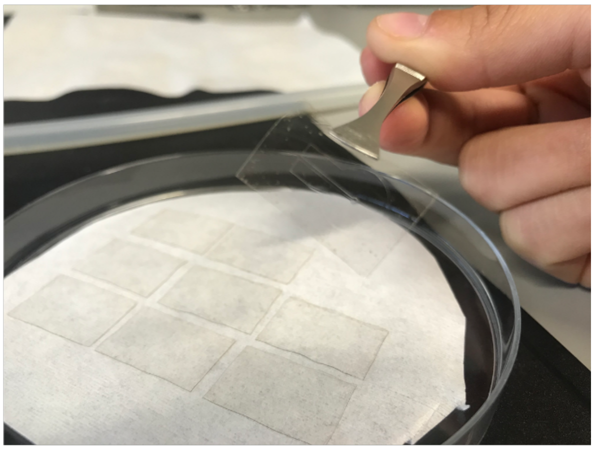

Figure 5.10: Rectangular shapes of molded PDMS for encapsulation.

The PDMS layers were subsequently treated with plasma to enhance the bonding. Once treated, the coil was manually aligned in the slot and the two 100 µm thick layers of PDMS were attached together with the coil inside. The SMA connectors were then attached to the exposed copper strip with silver paste. Even if the paste attachment is less strong than soldering, it was not possible to solder the SMA because the high temperature melts the PDMS.

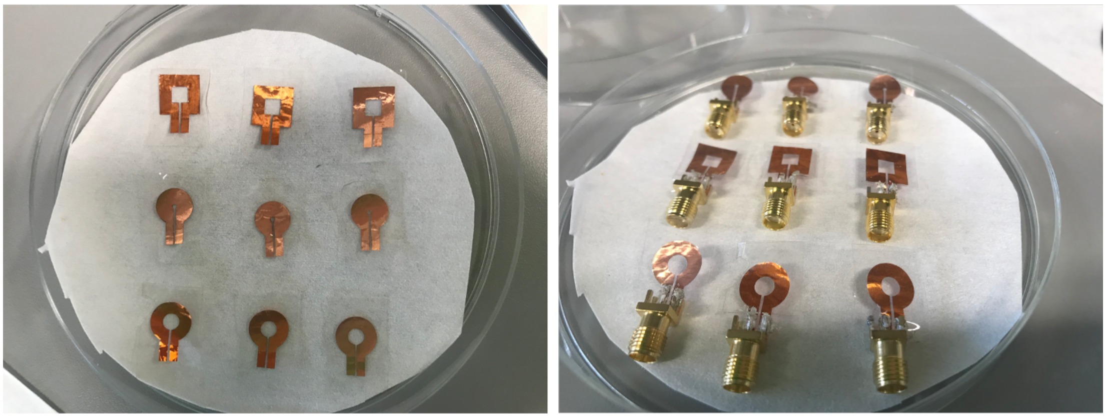

(a) (b)

Figure 5.11: (a) Fabricated coil resonators encapsulated in 200 µm of PDMS; (b) Coil resonators with SMA connector attached with silver paste.

The detailed process flow is reported in Appendix A.3.

5.3 Printed Coils Design

To generally test the IPT, some additional printed coils were designed in Altium and fabricated by Eurocircuits. The copper thickness is 35 µm while the FR4 substrate is 1.55 mm. All the fabricated coils are square shaped, but with different edge size and width (as displayed in Fig. 5.12). The SMA was assembled later on the exposed pads to perform the measurements.

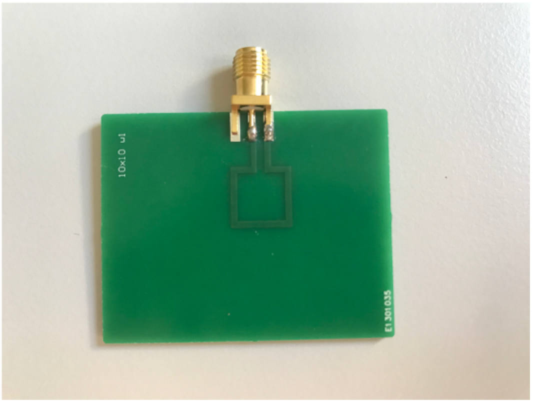

(a)

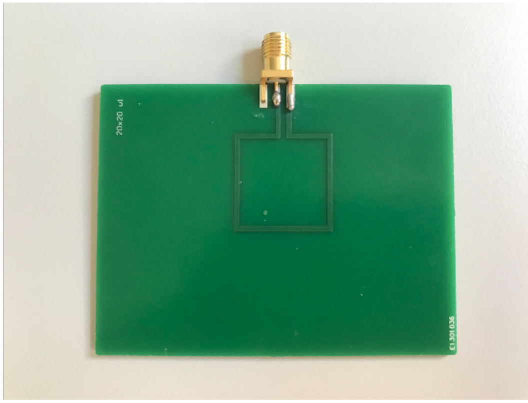

(b)

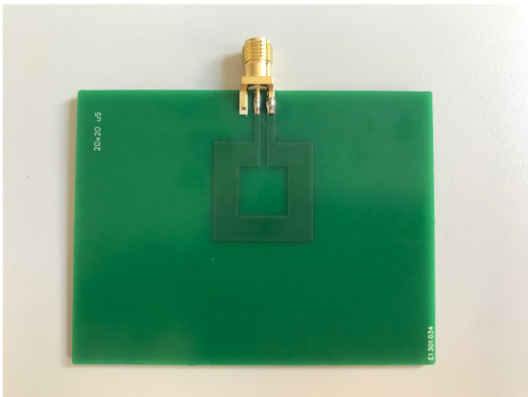

(c)

Figure 5.12: Printed square coils with SMA connectors. (a) 10 mm edge, 1 mm width; (b) 20 mm edge, 1 mm width; (c) 20 mm edge, 5 mm width.

Chapter 6

Inductive Power Transfer: Experimental Result

The microfabricated and printed coils were tested with the N5245A PNA-X Microwave Network Analyzer, characterized by a wide frequency range: from 10 MHz to 50 GHz. The station has four ports that can be calibrated with a Electronic Calibration (ECal) Kit. The performed measurements were done only with one port, in order to test the return loss (S11) of the single coil. However, with the instrument it is possible to measure also the overall inductive link, using two ports and, if needed, matching the source and load impedance as explained in Section 2.2.2. The measurements setup is the one in Fig. 6.1.

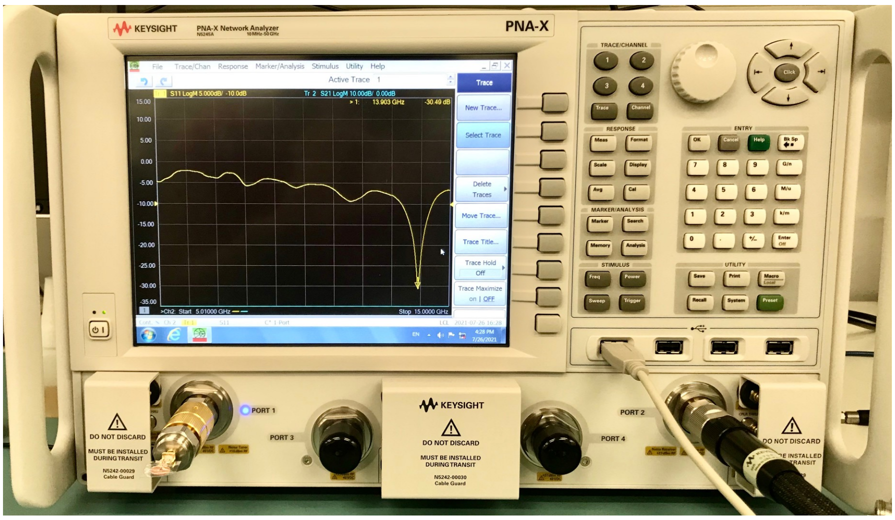

Figure 6.1: N5245A PNA-X Microwave Network Analyzer with resonator connected on port 1.

6.1 Microfabricated Resonator

The process flow gave the expected results. The PDMS layers were bonded together but a more effective bond can be reached by increasing the surface of the PDMS which, in the built structure, was limited due to the high density of SU-8 molds in the same wafer. The sputtered Si did not actually visibly improve the bonding of the materials and it is better to do not place it, to avoid a possible change of the magnetic properties.
The overall structure is flexible.
When measuring the return loss of the coils, the instrument returns a *csv* file with the real and imaginary part of S11. The S11 (dBm) vs. frequency plot is obtained with matlab, with the code reported in Appendix A.4.
To verify that the fabricated coil give the same results as the Ansys simulations, the exact fabricated coil was designed and simulated in air and without any presence of tissues, since also the measurements can only be done in air. The bottom layer of the modeled PDMS contains a slot of the same volume of the copper coil to reproduce the mold.
The Ansys model is shown in Fig. 6.2.

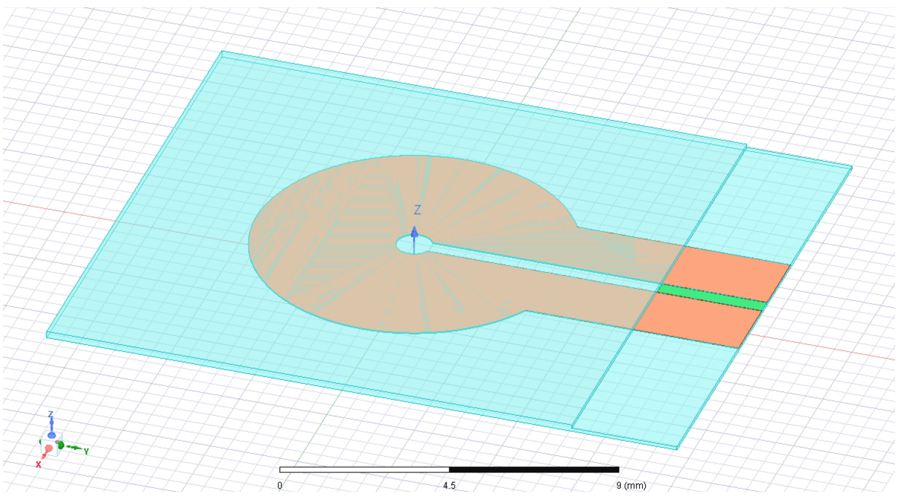

Figure 6.2: Ansys model of the fabricated resonator coil.

The comparison between the measured S11 of the fabricated circular coil and the simulated one is reported in Fig. 6.3.

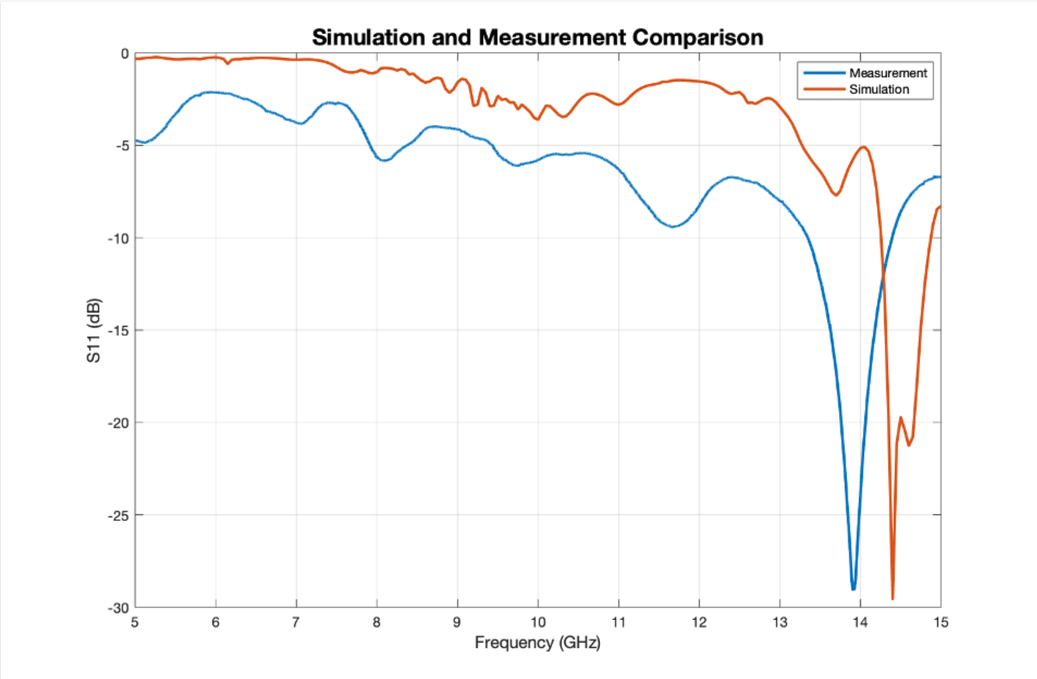

Figure 6.3: Comparison between measured and simulated S11 of the microfabricated resonator.

The trends of the simulated and measured S11 are equal one to the other but slightly shifted (approximately 0.5 GHz). The complete equality cannot be easily reached because any parameter strongly influences the measurements especially the presence of the SMA connector with the silver paste and the surrounding environment of the laboratory.

6.2 Printed Coils

As already done for the microfabricated resonator, one of the printed coil was modeled in air on Ansys to see if there was correspondence between the real coils and the simulations. The modeled coil is the one with 10 mm edge and 1 mm width. The substrate used is FR4 with relative permittivity of 4.4. The model is shown in Fig. 6.4.

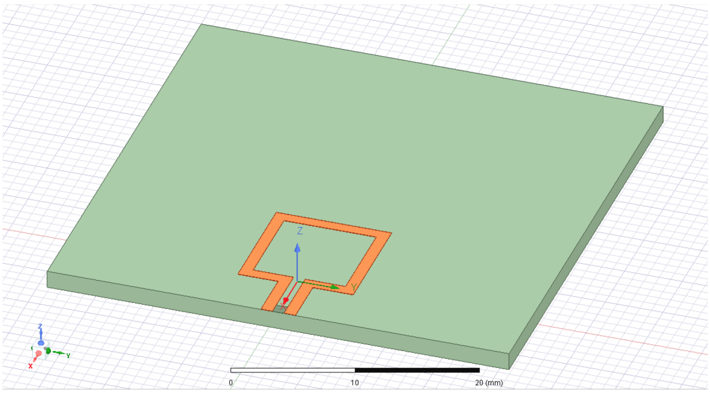

Figure 6.4: Ansys model of the printed coil.

The comparison between the printed coil and its simulation is reported in Fig. 6.5. The S11 minimum peak of both plots is in the same frequency range (6.4 GHz to 6.8 GHz) and the trend is similar. The differences are attributed again to the environment which influences the measurement and to the unknown exact shape and parameters of the solder mask, present on the coil manufactured by Eurocircuits that was neglected in the simulation.

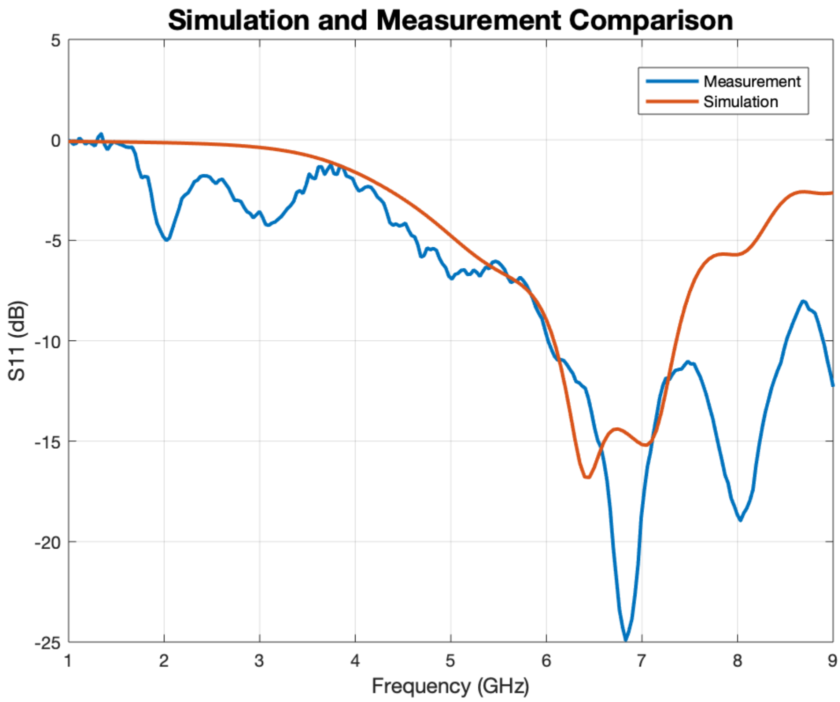

Figure 6.5: Comparison between measured and simulated S11 of the printed coil.

An overall picture of the PCB tested together with both the printed and resonator coils is shown in Fig. 6.6.

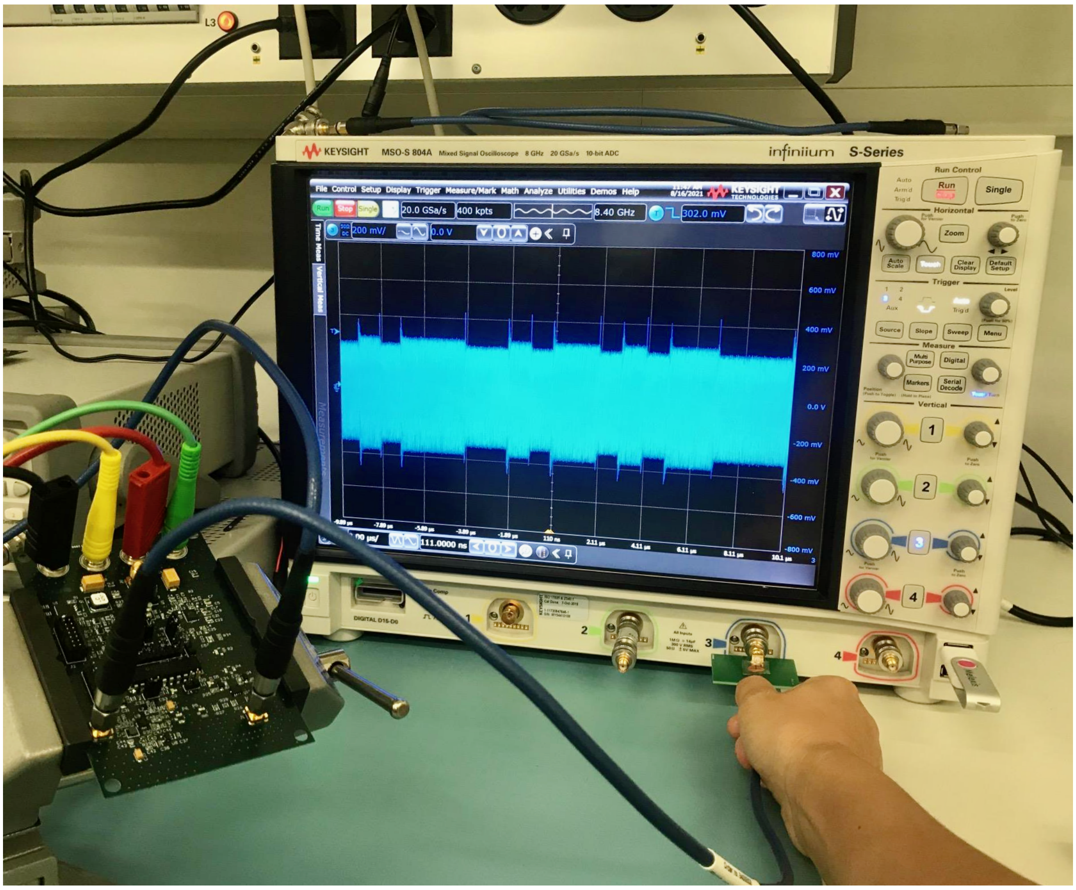

Figure 6.6: Overview of the transmitting system composed by PCB and printed coil and the fabricated resonator.

Chapter 7

Future Developments

7.1 New PCB Prototype

From the results obtained from the first PCB prototype, a new prototype was designed removing the unnecessary parts and adjusting the reflections. The main changes are:

- Remove the interface to connect the external programming board for setting the registers of the PLL, since the setting through the microcontroller was successful.

- Add another switch at the end of the T-Pad and the not attenuated trace in order to avoid any intersection of the traces leading to reflections.

Moreover, the additional connectors placed to be able insert the signal from outside were removed as well of the header to set the PLL in MUTE mode, that was found useless if the SPI signals are sent directly from the MCU.
The footprints for the capacitors in the Pierce oscillator were kept, in order to have always the possibility to solder any capacitance if needed.
Since the M3SW-2-50DRA+ switch is bi-directional, and it is extremely important to have both switches moving at the exact same time, another M3SW-2-50DRA+ was placed after the T-Pad attenuator and the not attenuated trace in order to have the configuration in Fig. 7.1. With the two switches controlled by the same digital signal, the RF signal travels exclusively through one of the two traces, either the attenuating or the non-attenuating one, avoiding any intersection between them.

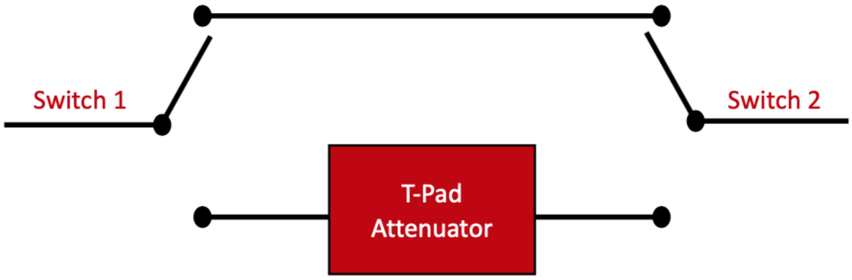

Figure 7.1: Amplitude-Shift Keying with double switch.

The new PCB schematic for future manufacturing is shown in Fig. 7.2.

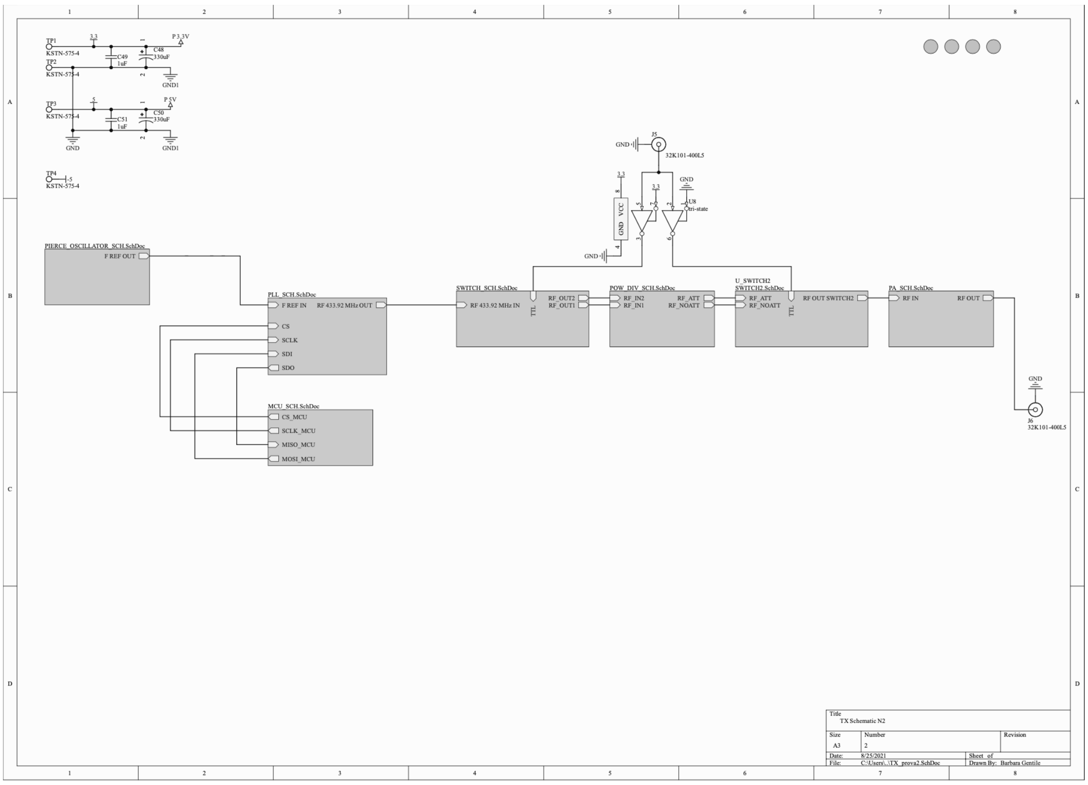

Figure 7.2: Schematic of improved PCB.

Placing the switches in this way, and controlling them with the same digital signal, the position of the short circuit of the first switch is opposite to the short circuit of the second one. Hence, if the switches are controlled by the same signal, there is no way to do not overlap two traces, which is not adequate for RF signals. To solve the issue, a dual buffer/driver as the SN74LVC2G240 by Texas Instrument can be exploited to have, with the same propagation delay time, a buffered and an inverted digital signal, to give respectively as input to the first and second switch. With the chosen dual buffer/driver, the output is buffered if, with a power voltage of 3.3 V, the enable signal is higher than 2 V and inverted if lower than 2 V. Giving as enable signals respectively 3.3 V and 0 V, the first and the second switches are controlled by opposite signals avoiding the crossing of the traces.
Another improvement that has been done in the layout is to place all the RF components on a single line, to avoid any curve of the traces.
The new 3D model of the layout, ready for manufacturing and assembly is the one in Fig. 7.3.

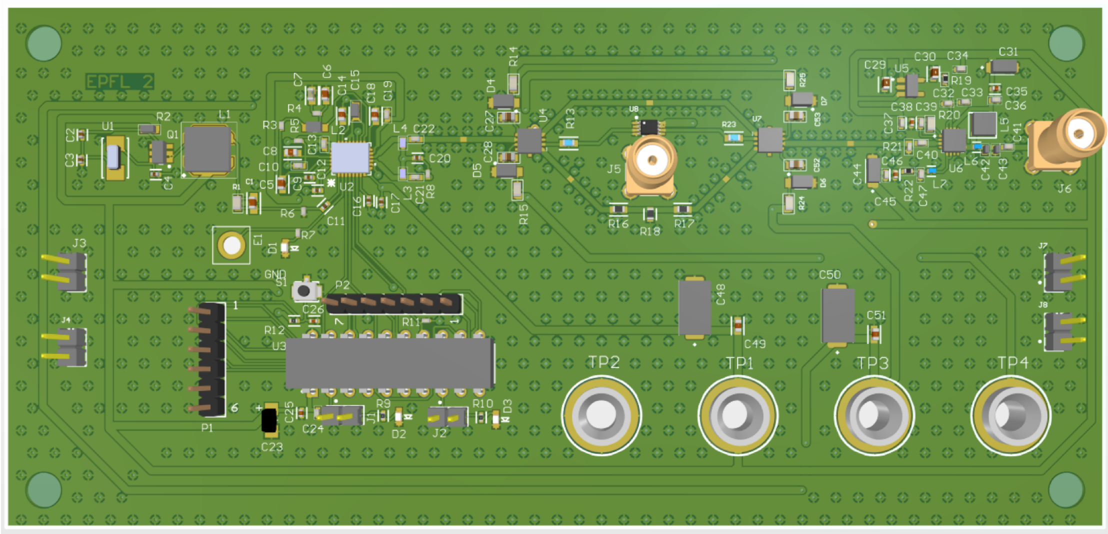

Figure 7.3: 3D model of the new PCB prototype.

The final improvement that will be done, at a second stage, is to build a flexible PCB for better comfort of the patient.

7.2 PCB Power Supply

In the future, the PCB will be not powered by generator, indeed the overall system of camera and PCB will be powered by a rechargeable battery providing a unique voltage. All the other needed voltages for the PCB will be given to the circuits through voltage regulators.
The power needed for the circuit is, currently, 2.59 W.
Lithium-Ion batteries at 3.7 V seem to be the most suitable in terms of energy density and also the most used. Assuming that the time that a person is awake during the day is around 17 hours, 44,030 mW h are needed to use the device the whole day, which corresponds to 11,900 mA h. With a Lithium-Ion battery system at 3.7 V that provides 11,900 mA h, the transmitter will work continuously for the whole day. Concerning the voltage regulators, if a 3.7 V battery is used, they will be needed for all the requested voltages in the circuit: 2.8 V, 3.3 V, 5 V, −5 V. The one for the 2.8 V has already been used in the first PCB prototype: the LDO TPS7A2028PDBVR by Texas Instrument, suitable for low load currents. Concerning the 3.3 V, 5 V and −5 V, a switching regulator is needed because it is characterized by high efficiency and it allows to achieve output voltages higher than the input. For the 5 V and −5 V, the LT3582-5 by Analog Devices is adequate since its input range is 2.55 V to 5.5 V and the output currents are: for the negative voltage 125 mA (only 4 mA are needed considering the two switches), while for the positive voltage 150 mA (the actual current used is 40 mA and cannot go over 80 mA with two switches). A suitable voltage regulator for the 3.3 V is TPS6208833YFP by Texas Instrument with input range of 2.55 V to 5.5 V and output current up to 3 A, while the present output current is 722 mA.

7.3 Further Optimization of the Inductive Link

Concerning the coils, starting from the optimization and fabrication process of the resonator, a further study with the three coils all together can be done both in air and in the tissues to maximise the PDL and PTE, knowing that the parameters obtained in the tissues cannot be tested, but the ones simulated in air can be checked using the network and spectrum analyzer. The whole IPT link can be tested in air, with both the optimized printed coil and resonator and the receiving coils of the chip. All the LC tanks should be tuned at 433.92 MHz to obtain the best PTE and PDL.

Chapter 8

Conclusions

Implantable prosthetic devices are a dream that has recently become true. The fabrication techniques are improving every day, giving the possibility to implant super-miniaturized devices acting on the neural system with little invasive surgeries. Neural implants can help diagnose and treat a wide range of brain pathologies. Among the brain implants, the sensory substitution is, with no doubt, one of the most astonishing applications. Acting on the cortex to restore vision, as the aim of this project, allows to treat any reason of visual impairment such as retinal diseases, glaucoma, optic atrophy or traumatic damages.
In-brain biomedical implants are challenging. One of the greatest advantage of this project is the development of a totally wireless system that allows to avoid any kind of wire implantation that, besides being very invasive for the patient, can easily lead to scarring and infections. The work that has been done in the thesis, the PCB transmitter and the optimization and fabrication of the inductive link is a significant step for the achievement of the wireless transmission.
Through the 3-coil wireless link and ASK modulation of the sinusoidal wave in the 433.92 MHz band, it is possible to transmit information while continuously powering the implants. The first PCB prototype gives already good results since all the blocks work as desired and the overall output, besides little attenuations, is the expected one. With the PCB improvements, explained in Section 7, the overall output will be further optimized and the PCB will be close the final flexible one. The coils simulations gave promising results in terms of quality factors and the fabrication process allowed to obtained the desired test configuration. The overall work was fundamental for the project to obtain a complete wireless transmission of data and power to the super-miniaturized CMOS µelectrodes and, in general, for the improvement of any implanted device that can be powered from the outside, reducing the invasivity of the implants.

Appendix A

Additional Content

A.1 Additional Equations for Impedance Calculation

Auxiliary equations for calculation of the effective permittivity in a microstrip.

$$a_u = 1 + \frac{1}{49} \ln \left(\frac{u_r^4 + \frac{u_r^2}{2704}}{u_r^4 + 0.432} \right) \Big| + \frac{1}{18.7} \ln \left[1 + \left(\frac{u_r}{18.1} \right)^3 \right] \tag{A.1}$$

$$b_\varepsilon = 0.564 \left(\frac{\varepsilon_r - 0.9}{\varepsilon_r + 3} \right)^{0.053} \tag{A.2}$$

A.2 Code Composer Studio for MSP430

Code for MCU programming to set the register of the PLL through the SPI interface.

```c
#include <msp430.h>

char packet[] = {0x02, 0b00000100, 0b00000100, 0b00111110, 0b00101100, 0b00000001, 0b00001000, 0b11000000, 0b00000000, 0b00000000, 0b00010000, 0b11111110, 0b00101101, 0b00000000};

unsigned int position;

/**
 * main.c
 */

```

```
int main(void)
{
        WDTCTL = WDTPW | WDTHOLD; // Stop watchdog timer

        UCB0CTL1 |= UCSWRST;
        UCB0CTL1 |= UCSSEL_2; // SMCLK 1MHz

        UCB0BR0 = 6; // Prescaler to obtain 6us clock period

        UCB0CTL0 |= UCSYNC; // Put into SPI (syncronous)
        UCB0CTL0 |= UCMST; // Put into SPI Master
        UCB0CTL0 |= UCMSB; // MSB first
        UCB0CTL0 |= UCMODE_1; // 4 pin spi
        UCB0CTL0 |= UCCKPH; // Clock polarity 1

//-- SET TIMER_A FOR COMMUNICATION START (START WHEN OVERFLOW)

        TA0CTL |= TACLR; // Reset timer
        TA0CTL |= TASSEL_2; // Clock = smclk
        TA0CTL |= ID_3; // Clock divided by 8
        TA0CTL |= MC_2; // Continuous up mode

        //-- Port config

        P1SEL |= BIT5; // P1.5 use SCLK
        P1SEL2 |= BIT5;

        P1SEL |= BIT6; // P1.6 use MISO
        P1SEL2 |= BIT6;

        P1SEL |= BIT7; // P1.7 use MOSI
        P1SEL2 |= BIT7;

        P1DIR |= BIT4; // CS signal high
        P1OUT |= BIT4;

        //Config LED

        P1DIR |= BIT0;
        P1OUT &= ~BIT0; // Start with led off

        UCB0CTL1 &= ~UCSWRST; // Take out software reset

//-- Enable IRQs

        //--Setup ta0 overflow irq

        TA0CTL |= TAIE; // Local enable for ta0 overflow
        TA0CTL &= ~TAIFG; // Clear flag
```

```

        IE2 |= UCB0TXIE; // Enable B0 tx IRQ
        IFG2 &= ~ UCB0TXIFG; // Clear flag


        __enable_interrupt(); // Enable global

        while(1){}

    return 0;
}

#pragma vector = TIMER0_A1_VECTOR // A1 because it is the second
    timer
__interrupt void ISR_TA0_Overflow(void){
    P1OUT &= ~BIT4; // CS signal low
    P1OUT |= BIT0; // Led is on --> Start of communication
    position = 0;
    UCB0TXBUF = packet[position]; // Send first byte
    TA0CTL &= ~TAIFG; // Clear flag
    TA0CTL &= ~TAIE; // Disable interrupt
}

#pragma vector = USCIAB0TX_VECTOR ;
__interrupt void ISR_USCI_B0(void){
    P1OUT &= ~BIT4;
    position ++;
    TA0CTL &= ~TAIFG; // Clear flag

    if(position < sizeof(packet)){
        UCB0TXBUF = packet[position]; // New packet in trasmission
    buffer
    }
    else
    {
        IFG2 &= ~ UCB0TXIFG; // Clear flag
        P1OUT &= ~BIT0; // Led is off
        int i;
        for(i=0;i<2;i++){}
        P1OUT |= BIT4;
    };
}
```

A.3 Process Flow Coil

Process flow for the fabrication of the resonator coil in cleanroom at Wyss Center of Campus Biotech.

Lab : EPFL LNE
Operateur Name :
Barbara Gentile
Supervisor Name :
Diego Ghezzi

Process Flow

Inductive link for cortical visual prosthesis

Description

Copper coil in PDMS substrate for inductive link.

Neural Microsystems Platform's machine needed
Laser cutter, Mixer, Defoamer, Spin coater, Hotplate, Oven, MLA, Sputter, Profilometer
Substrate Type
Wafer 4 inch (qty:2)

Process Outline

01	**Laser cutting** **Machine:** Laser cutter **Material:** Copper 25um **Parameters**: Speed 100, Power 60, Rep Obj 110	
02	**Amorphous Si Sputter** (OPTIONAL) **Thickness:** 10 nm on both sides OPTIONAL FOR BETTER ADHESION (did not actually improved the adhesion)	

Lab : EPFL LNE
Operateur Name :
Barbara Gentile
Supervisor Name :
Diego Ghezzi

WYSS CENTER for Bio- and Neuro-Engineering

03	**<u>Spin coating SU8</u>** **Thickness:** 25 um **Material:** 1070 15-200um **Rpm:** 3000 rpm for 40 s	
04	**<u>Soft bake</u>** **Recipe:** SU8 1070 RECIPE	
05	**<u>Exposure</u>** **Machine:** MLA **Parameter:** RECIPE	
06	**<u>Post exposure bake</u>** **Recipe:** SU8 1070 RECIPE	
07	**<u>Development and hard bake</u>**	

08	**<u>Profilometer measurements</u>** **Machine:** profilometer (to see if correct thickness)	
09	**<u>Spin Coating release layer (PSS)</u>** **Machine:** spin coater **Rpm:** Standard 1000	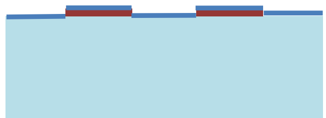
10	**<u>Cure PSS</u>** **Machine:** Hotplate **Temperature and Time:** 145 C, 10 min	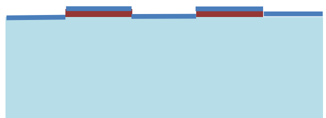
11	**<u>Spin coating PDMS</u>** **Thickness:** 100 um **Rpm:** RECIPE **Ratio:** 9:1 **Machine**: Mixer, Spin coater	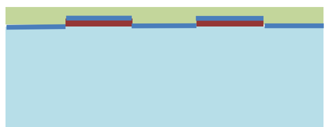
12	**<u>PDMS Curing</u>** **Machine:** Oven, 75 C, 2 hours	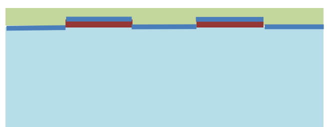

13	**<u>Release DI</u>**	
14	**<u>Spin Coating release layer (PSS)</u>** **<u>(on second wafer)</u>** **Machine:** spin coater **Rpm:** Standard 1000	
15	**<u>Cure PSS</u>** **<u>(on second wafer)</u>** **Machine:** Hotplate **Temperature and Time:** 145 C, 10 min	
16	**<u>Spin coating PDMS</u>** **<u>(on second wafer)</u>** **Thickness:** 100 um **Rpm:** RECIPE **Ratio:** 9:1 **Machine:** Mixer, Defoaming, Spin coater	

17	**<u>Curing PDMS</u>** **<u>(on second wafer)</u>** **Machine:** Oven **Time and temperature:** 75 C, 2 hours	
18	**<u>Cutter</u>** **<u>(on second wafer)</u>** **Machine:** Laser cutter	
19	**<u>Release in DI</u>** **<u>(on second wafer)</u>**	
20	**<u>Plasma treatment and attachment</u>**	

After the attachment the encapsulated coil was placed on the hotplate with a small weight to enhance the attachment.

A.4 S11 Plot

The S11 plots of both the measurements and simulations are obtained from the *csv* files imported in matlab. While Ansys reports directly the value in dBm of the S parameters, the N5245A Network Analyzer gives the imaginary and real parts of S that must be converted as shown in the code.

```
data_meas = readmatrix('Measure.csv'); % measured data estraction
data_sim = readmatrix('Simulation.csv'); % simulated data estraction

S11 = sqrt(data_meas(:,2).^2 + data_meas(:,3).^2); % S11 from Real
    and Imaginary parts
S11dB = 20*log10(S11); % S11 in dB

plot(data_meas(:,1).*10^-9,S11dB, 'LineWidth',2) % plot measured S11
    in GHz

hold on
grid on

plot(data_sim(:,2),data_sim(:,3), 'LineWidth',2) %plot simulated S11

xlabel("Frequency (GHz)",'FontSize',12)
ylabel("S11 (dB)",'FontSize',12)
legend ('Measurement', 'Simulation')
title ('Simulation and Measurement Comparison', 'FontSize',16)
```

Bibliography

[1] Gian Luca Barbruni, Fabio Asti, Paolo Motto Ros, Diego Ghezzi, Danilo Demarchi, and Sandro Carrara. «A 20 Mbps, 433 MHz RF ASK Transmitter to Inductively Power a Distributed Network of Miniaturised Neural Implants». In: *2021 IEEE International Symposium on Medical Measurements and Applications (MeMeA)*. June 2021, pp. 1–6. DOI: `10.1109/MeMeA52024.2021.9478678` (cit. on pp. viii, 5, 22, 25, 31).

[2] Kateryna Bazaka and Mohan Jacob. «Implantable Devices: Issues and Challenges». In: *Electronics* 2 (Mar. 2012), pp. 1–34. DOI: `10.3390/electronics2010001` (cit. on pp. 1, 4).

[3] Yeun-Ho Joung. «Development of implantable medical devices: from an engineering perspective». In: *International Neurourology Journal* 17.3 (Sept. 2013), pp. 98–106. ISSN: 2093-4777. DOI: `10.5213/inj.2013.17.3.98` (cit. on p. 1).

[4] K.D. Wise, D.J. Anderson, J.F. Hetke, D.R. Kipke, and K. Najafi. «Wireless implantable microsystems: high-density electronic interfaces to the nervous system». In: *Proceedings of the IEEE* 92.1 (Jan. 2004). Conference Name: Proceedings of the IEEE, pp. 76–97. ISSN: 1558-2256. DOI: `10.1109/JPROC.2003.820544` (cit. on p. 2).

[5] J. M. Kahn, R. H. Katz, and K. S. J. Pister. «Next century challenges: mobile networking for "Smart Dust"». In: *Proceedings of the 5th annual ACM/IEEE international conference on Mobile computing and networking - MobiCom '99*. Seattle, Washington, United States: ACM Press, 1999, pp. 271–278. ISBN: 978-1-58113-142-0. DOI: `10.1145/313451.313558` (cit. on p. 2).

[6] Dongjin Seo, Jose M. Carmena, Jan M. Rabaey, Elad Alon, and Michel M. Maharbiz. «Neural Dust: An Ultrasonic, Low Power Solution for Chronic Brain-Machine Interfaces». In: (July 2013). arXiv: 1307.2196. URL: `http://arxiv.org/abs/1307.2196` (cit. on p. 2).

[7] Sandro Carrara. «Body Dust: Well Beyond Wearable and Implantable Sensors». In: *IEEE Sensors Journal* 21.11 (June 2021). Conference Name: IEEE Sensors Journal, pp. 12398–12406. ISSN: 1558-1748. DOI: 10.1109/JSEN.2020.3029432 (cit. on p. 2).

[8] E. Fernández, F. Pelayo, S. Romero, M. Bongard, C. Marin, A. Alfaro, and L. Merabet. «Development of a cortical visual neuroprosthesis for the blind: the relevance of neuroplasticity». In: *Journal of Neural Engineering* 2.4 (Dec. 2005). ISSN: 1741-2560. DOI: 10.1088/1741-2560/2/4/R01 (cit. on p. 2).

[9] Rupert Bourne et al. «Trends in prevalence of blindness and distance and near vision impairment over 30 years: an analysis for the Global Burden of Disease Study». In: *The Lancet Global Health* 9.2 (Feb. 2021). Publisher: Elsevier. ISSN: 2214-109X. DOI: 10.1016/S2214-109X(20)30425-3 (cit. on p. 2).

[10] William Watson. «An account of Mr. Benjamin Franklin's treatise, lately published, intituled, Experiments and observations on electricity, made at Philadelphia in America». en. In: *Philosophical Transactions of the Royal Society of London* 47 (Dec. 1752), pp. 202–211. ISSN: 0261-0523, 2053-9223. DOI: 10.1098/rstl.1751.0032 (cit. on p. 2).

[11] J. O. Mills, A. Jalil, and P. E. Stanga. «Electronic retinal implants and artificial vision: journey and present». In: *Eye (London, England)* 31.10 (Oct. 2017), pp. 1383–1398. ISSN: 1476-5454. DOI: 10.1038/eye.2017.65 (cit. on p. 2).

[12] Wm H. Dobelle, Michael G. Mladejovsky, Jerald R. Evans, T. S. Roberts, and J. P. Girvin. «'Braille' reading by a blind volunteer by visual cortex stimulation». In: *Nature* 259.5539 (Jan. 1976). re, pp. 111–112. ISSN: 1476-4687. DOI: 10.1038/259111a0 (cit. on p. 3).

[13] Philip Lewis, Helen Ackland, Arthur Lowery, and Jeffrey Rosenfeld. «Restoration of vision in blind individuals using bionic devices: A review with A focus on cortical visual prostheses». In: *Brain Research* 1595 (Jan. 2015), pp. 51–73. DOI: 10.1016/j.brainres.2014.11.020 (cit. on p. 3).

[14] Diego Ph D. Ghezzi. «Retinal prostheses: progress toward the next generation implants». In: *Frontiers in Neuroscience* (2015). Publisher: Frontiers. ISSN: 1662-453X. DOI: 10.3389/fnins.2015.00290 (cit. on p. 3).

[15] Rick Hartley. *RF / Microwave PC Board Design and Layout*. URL: https://www.jlab.org/accel/eecad/pdf/050rfdesign.pdf (cit. on pp. 7, 9).

[16] *The 50 Ω Question: Impedance Matching in RF Design | Real-Life RF Signals | Electronics Textbook*. URL: https://www.allaboutcircuits.com/textbook/radio-frequency-analysis-design/real-life-rf-signals/the-50-question-impedance-matching-in-rf-design/ (cit. on p. 8).

[17] Orta Renato. *Teoria delle Linee di Trasmissione*. Mar. 1999 (cit. on pp. 8, 9).

[18] *The IPC-2252, Design Guide for RF/Microwave Circuit Boards*. July 2002 (cit. on pp. 10, 11).

[19] *7.19 Frequency Variation of the Characteristic Impedance | The Physical Basis of Transmission Lines | InformIT*. URL: `https://www.informit.com/articles/article.aspx?p=2916283&seqNum=19` (cit. on p. 11).

[20] *Transmission Line Impedance Calculation With Altium Designer 20 | Altium*. URL: `https://resources.altium.com/webinars/transmission-line-impedance-calculation-with-altium-designer-20` (cit. on p. 12).

[21] S. Abdollah Mirbozorgi, Pyungwoo Yeon, and Maysam Ghovanloo. «Robust Wireless Power Transmission to mm-Sized Free-Floating Distributed Implants». In: *IEEE Transactions on Biomedical Circuits and Systems* 11.3 (June 2017). Conference Name: IEEE Transactions on Biomedical Circuits and Systems, pp. 692–702. ISSN: 1940-9990. DOI: `10.1109/TBCAS.2017.2663358` (cit. on pp. 13, 17).

[22] Gian Barbruni, Paolo Motto Ros, Sandro Carrara, and Diego Ghezzi. «Miniaturised Wireless Power Transfer Systems for Neurostimulation: A Review». In: *IEEE Transactions on Biomedical Circuits and Systems* PP (Dec. 2020). DOI: `10.1109/TBCAS.2020.3038599` (cit. on p. 13).

[23] Byunghun Lee, Mehdi Kiani, and Maysam Ghovanloo. «A Triple-Loop Inductive Power Transmission System for Biomedical Applications». In: *IEEE Transactions on Biomedical Circuits and Systems* 10.1 (Feb. 2016). Conference Name: IEEE Transactions on Biomedical Circuits and Systems, pp. 138–148. ISSN: 1940-9990. DOI: `10.1109/TBCAS.2014.2376965` (cit. on p. 14).

[24] S. A. Mirbozorgi, B. Gosselin, and M. Sawan. «A transcutaneous power transfer interface based on a multicoil inductive link». In: *2012 Annual International Conference of the IEEE Engineering in Medicine and Biology Society*. ISSN: 1558-4615. Aug. 2012, pp. 1659–1662. DOI: `10.1109/EMBC.2012.6346265` (cit. on pp. 14, 17).

[25] Mehdi Kiani, Uei-Ming Jow, and Maysam Ghovanloo. «Design and Optimization of a 3-Coil Inductive Link for Efficient Wireless Power Transmission». In: *IEEE Transactions on Biomedical Circuits and Systems* 5.6 (Dec. 2011). Conference Name: IEEE Transactions on Biomedical Circuits and Systems, pp. 579–591. ISSN: 1940-9990. DOI: `10.1109/TBCAS.2011.2158431` (cit. on pp. 14, 15, 18).

[26] Michael W. Baker and Rahul Sarpeshkar. «Feedback Analysis and Design of RF Power Links for Low-Power Bionic Systems». In: *IEEE Transactions on Biomedical Circuits and Systems* 1.1 (Mar. 2007). Conference Name: IEEE Transactions on Biomedical Circuits and Systems, pp. 28–38. ISSN: 1940-9990. DOI: 10.1109/TBCAS.2007.893180 (cit. on p. 15).

[27] Pyungwoo Yeon, S. Abdollah Mirbozorgi, and Maysam Ghovanloo. «Optimal design of a 3-coil inductive link for millimeter-sized biomedical implants». In: *2016 IEEE Biomedical Circuits and Systems Conference (BioCAS)*. Oct. 2016, pp. 396–399. DOI: 10.1109/BioCAS.2016.7833815 (cit. on pp. 18, 19).

[28] Weiwei Ye, Lu Chen, Fuxin Liu, Xuling Chen, and Xuehua Wang. «Analysis and optimization of 3-coil magnetically coupled resonant wireless power transfer system for stable power transmission». In: *2017 IEEE Energy Conversion Congress and Exposition (ECCE)*. Oct. 2017, pp. 2584–2589. DOI: 10.1109/ECCE.2017.8096490 (cit. on p. 18).

[29] Fabian L. Cabrera, Renato S. Feitoza, and F. Rangel de Sousa. «Extending the inductor operating frequency for optimally-coupled wireless power transfer systems». In: *2015 SBMO/IEEE MTT-S International Microwave and Optoelectronics Conference (IMOC)*. Nov. 2015, pp. 1–5. DOI: 10.1109/IMOC.2015.7369105 (cit. on p. 19).

[30] S. Abdollah Mirbozorgi, Yaoyao Jia, and Maysam Ghovanloo. «Power Efficiency and Power Delivery Measurement in Inductive Links with Arbitrary Source and Load Impedance Values». In: *2018 IEEE Life Sciences Conference (LSC)*. Oct. 2018, pp. 25–28. DOI: 10.1109/LSC.2018.8572077 (cit. on p. 20).

[31] *Tips for Coil users*. URL: https://www.sagami-elec.co.jp/file/tech/coil_doc_100e.pdf (cit. on p. 21).

[32] Matthew Schormans, Virgilio Valente, and Andreas Demosthenous. «Practical Inductive Link Design for Biomedical Wireless Power Transfer: A Tutorial». In: *IEEE Transactions on Biomedical Circuits and Systems* 12.5 (Oct. 2018). Conference Name: IEEE Transactions on Biomedical Circuits and Systems, pp. 1112–1130. ISSN: 1940-9990. DOI: 10.1109/TBCAS.2018.2846020 (cit. on p. 21).

[33] Adam Khalifa, Yasha Karimi, Qihong Wang, Sahithi Garikapati, Webert Montlouis, Milutin Stanaćević, Nitish Thakor, and Ralph Etienne-Cummings. «The Microbead: A Highly Miniaturized Wirelessly Powered Implantable Neural Stimulating System». In: *IEEE Transactions on Biomedical Circuits and Systems* 12.3 (June 2018). Conference Name: IEEE Transactions on Biomedical Circuits and Systems, pp. 521–531. ISSN: 1940-9990. DOI: 10.1109/TBCAS.2018.2802443 (cit. on p. 21).

[34] Barry N Breen, Chaim Goldberger, and Leonid Talalaevsky. *The Accu-L Multi-Layer Inductor for High Frequency Applications | AVX*. Dec. 2013. URL: https://www.avx.com/docs/techinfo/RFMicrowaveThinFilm/aculmlc.pdf (cit. on p. 22).

[35] «IEEE Standard for Safety Levels with Respect to Human Exposure to Radio Frequency Electromagnetic Fields, 3 kHz to 300 GHz». In: *1, 1999 Edition IEEE Std C95* (Apr. 1999). Conference Name: 1, 1999 Edition IEEE Std C95, pp. 1–83. DOI: 10.1109/IEEESTD.1999.89423 (cit. on p. 22).

[36] Andreas Christ, Mark Douglas, Jagadish Nadakuduti, and Niels Kuster. «Assessing Human Exposure to Electromagnetic Fields From Wireless Power Transmission Systems». In: *Proceedings of the IEEE* 101.6 (June 2013). Conference Name: Proceedings of the IEEE, pp. 1482–1493. ISSN: 1558-2256. DOI: 10.1109/JPROC.2013.2245851 (cit. on p. 22).

[37] *What are the ISM Bands, and What Are They Used For? | Military Aerospace*. URL: https://www.militaryaerospace.com/directory/blog/14059677/what-are-the-ism-bands-and-what-are-they-used-for (cit. on p. 22).

[38] *Guidelines for Use of ISM Bands*. Feb. 2014. URL: https://www.motc.gov.qa/en/documents/document/guidelines-use-ism-bands (cit. on p. 22).

[39] *Frequency bands designated for Industrial, Scientific and Medical use (ISM)*. URL: https://www.ofcom.org.uk/__data/assets/pdf_file/0022/103297/fat-ism-frequencies.pdf (cit. on p. 22).

[40] Nur Ahmadi et al. «Towards a Distributed, Chronically-Implantable Neural Interface». In: San Francisco, CA, USA, Mar. 2019, pp. 719–724. DOI: 10.1109/NER.2019.8716998 (cit. on p. 23).

[41] *NX5032GA Series Datasheet*. URL: https://www.ndk.com/images/products/catalog/c_NX5032GA_e.pdf (cit. on p. 27).

[42] *LTC6948 Datasheet*. URL: https://www.analog.com/media/en/technical-documentation/data-sheets/6948fa.pdf (cit. on p. 27).

[43] *M3SW-2-50DRA+ Datasheet*. URL: https://www.minicircuits.com/pdfs/M3SW-2-50DRA+.pdf (cit. on p. 29).

[44] *T-pad Attenuator Tutorial for Passive Attenuators*. July 2013. URL: https://www.electronics-tutorials.ws/attenuators/t-pad-attenuator.html (cit. on p. 30).

[45] *Difference between 10% ASK modulation,100% ASK modulation*. URL: https://www.rfwireless-world.com/Terminology/10-ASK-modulation-vs-100-ASK-modulation.html (cit. on p. 31).

[46] *RF5110G Datasheet*. URL: https://www.mouser.it/datasheet/2/412/Qorvo_RF5110G_Data_Sheet-2507647.pdf (cit. on p. 31).

[47] *MSP430G2x53, MSP430G2x13 Mixed Signal Microcontroller Datasheet.* Apr. 2011. URL: https://www.ti.com/lit/ds/slas735j/slas735j.pdf?ts=1630506090757&ref_url=https%253A%252F%252Fwww.google.com%252F (cit. on p. 34).

[48] *Linear vs. Switching Regulators | Renesas.* URL: https://www.renesas.com/us/en/products/power-power-management/linear-vs-switching-regulators (cit. on p. 41).

[49] *Adding Via Stitching & Via Shielding to a PCB in Altium Designer | Altium Designer 21 User Manual | Documentation.* URL: https://www.altium.com/documentation/altium-designer/via-stitching-and-via-shielding-ad (cit. on p. 43).